Petrogenesis and tectonomagmatic significance of Eocene mafic intrusions from the Neo-Tethyan suture zone in the Muslim Bagh-Khanozai region, Pakistan

Andrew C. Kerr[1*], Owain Lavis[1], M. Ishaq Kakar[2], Iain McDonald[1]

[1] School of Earth and Ocean Sciences, Cardiff University, Main Building, Park Place, Cardiff, Wales, CF10 3AT, UK.

[2] Centre of Excellence in Mineralogy, University of Balochistan, Quetta, Pakistan.

* Corresponding author. *E-mail address: kerra@cf.ac.uk*

Words of text (excl refs): 5303

References: 52

Tables: 2

Figures: 13

Abbreviated title: *Tethyan suture zone intrusions*

Abstract

New geochemical data for mafic intrusions within the Eocene Nisai Formation along the suture zone between the Indian and Eurasian plates are used to constrain their petrogenesis and assess the local tectonics and mantle dynamics. Petrological and geochemical data indicates that these alkalic intrusions have moderately enriched incompatible trace element compositions similar to ocean island basalt (OIB) magmatism. Modelling suggests these intrusions are the result of 1-5% melting of a deep, enriched, predominantly garnet-lherzolite, with a small amount of subduction-derived fluids. These melts then underwent fractional crystallisation at lithospheric depths of ~30 km.

It is proposed that the Nisai intrusions were generated by decompression asthenospheric melting. This melting is likely to have been aided by residual (warmer) asthenosphere from the Réunion plume resulting in melting of a more-enriched mantle source over a range of depths and the formation of OIB-like melts. In common with other areas along the Neo-Tethyan suture zone, this melting was facilitated by subduction fluid release and slab detachment/tearing during continental collision. The hydrous melt pooled and fractionated within a magma chamber in the crustally thickened lithosphere (perhaps with a small amount of crustal assimilation) at approximately 30 km and was intermittently tapped resulting in the upward migration of melt and subsequent intrusion of the Nisai sills.

The Neo-Tethyan suture zone is marked by a series of ophiolitic complexes and sedimentary rocks which have helped to unravel the tectonomagmatic development, and subsequent collision, of the Indian and Eurasian plate margins (e.g., Dilek and Furnes, 2009). The ophiolites and other Jurassic-Cretaceous magmatic rocks particularly in the Muslim Bagh–Khanozai region of north-western Pakistan (Figure 1) have been the focus of recent detailed study (e.g., Mahmood et al., 1995; Mahoney et al., 2002; Khan et al., 2007; Kerr et al., 2010; Kakar et al., 2014).

In the Muslim Bagh-Khanozai region, mafic intrusions have recently been discovered in the Eocene Nisai Formation, part of the Flysch Belt of the collision zone (Figure 2). The Nisai intrusions are the youngest magmatic formations found thus far in the Muslim Bagh-Khanozai area, and therefore have the potential to provide fundamental information on the evolution of the Indian and Eurasian continental margins prior to, and during, continental collision.

This study presents a detailed petrological and geochemical study of the Nisai mafic intrusions in order to understand the nature of the mantle source, the depth of melting, magma chamber processes and why these magmatic rocks were generated in a collisional tectonic setting. In particular we will assess whether the melting responsible for these intrusions was a result of: subduction-related processes; localised decompression during continental collision (i.e., derived from an upper asthenosphere source similar to that of mid-ocean ridges); or elevated temperatures resulting from mantle plume-related activity associated with relatively enriched residual Réunion mantle plume material.

Tectonic Evolution and regional setting

The regional geology of Muslim Bagh-Khanozai region of Pakistan is intimately related to the collision of the Indian and Eurasian continents. The development of the Indian Ocean began

with the break-up of Gondwanaland. Madagascar-greater India initiated this breakup stage by rifting from Africa during the Late Jurassic-Early Cretaceous (Khan et al., 2007; Peters, 2000). It was during this period that the volcano-sedimentary Bagh Complex (see below) formed. After separation from Africa, the Indian plate began to rift from Madagascar during the Late Cretaceous, (~87–65 Ma) forming an oceanic spreading centre. This was associated with the rotation of the Indian continent and transpression along its north-western edge, resulting in the formation of short-lived incipient intra-oceanic subduction zones (e.g., Plummer, 1996). In the Late Cretaceous-Early Tertiary these supra-subduction zone rocks were subsequently obducted on to the northern and western margins of the Indian plate, (Gnos et al., 1997) to form the ophiolites of the Neo-Tethyan suture zone, including the Muslim Bagh- Khanozai ophiolite.

Continued north-directed subduction of Tethyan oceanic crust during the Late Cretaceous and early Tertiary eventually led to the collision of the Indian and Eurasian continents in the Early Eocene with final emplacement of the ophiolites onto the Indian continental passive margin (Beck et al., 1995). Collision of India with Eurasia was not simultaneous or uniform along the length of the margin, and the northern and eastern margins collided first in the Early-Mid Palaeocene (65–60 Ma) (e.g., Besse et al., 1984; Jaeger et al., 1989; Siddiqui et al., 1996; Bouilhol et al., 2013). This resulted in the dismembered and tectonised ophiolite melanges of the Himalayas. In contrast, ophiolites along the western suture zone ‘docked’ at a later stage (~40 Ma) with the Afghan continental block (Bouilhol et al., 2013). Unlike the northern and eastern margins, this docking occurred along transform faults, and so the ophiolite units are significantly less dismembered (Khan et al., 2007).

The Muslim Bagh, Khanozai, Bela, Zhob and Waziristan ophiolites formed part of the Neo-Tethyan Ocean, and are exposed along western suture zones between the Asian and Indian plates (Figure 1) (Asrarullah and Abbas, 1979). U-Pb dating of zircons from a plagiogranite in

the Muslim Bagh ophiolite has yielded an age 80.2 ± 1.5 Ma (Kakar et al., 2012); whereas ^{40}Ar-^{39}Ar dating of amphiboles from subophiolitic metamorphic rocks implies an ophiolite emplacement age of 68.7 ± 1.5 Ma (Mahmood et al., 1995; Kakar et al., 2014).

Regional Geology

Regional geology of the Muslim Bagh-Khanozai (Figure 1) region can be broadly divided into four zones, a passive margin, the Muslim Bagh-Khanozai ophiolites, the Bagh complex and a Flysch belt. The Flycsh belt contains the igneous intrusions in the present study.

Indian passive margin sediments are found stratigraphically beneath the Bagh Complex and consist of mostly shales and limestones, ranging in age from Triassic to Eocene (Durrani et al., 2012). The Gwal-Bagh Thrust separates the passive margin sediments from the Bagh Complex which is a Cretaceous sedimentary, igneous and metamorphic melange zone (Figure 1) (Siddiqui *et al.,* 1996; Kakar et al., 2014). The sedimentary units of the Bagh Complex were deposited on the continental margin of the Indian plate, while volcanic units are likely to have formed part of the Neo-Tethyan oceanic crust (Siddiqui et al., 1996; Kakar et al., 2014). Units of the Bagh Complex were scrapped off during oblique collision and obducted onto the northwestern margins of the Indian plate (Mengal et al., 1994; Siddiqui et al., 1996; Kakar et al., 2014).

The Muslim Bagh-Khanozai ophiolite complex overlies the Bagh complex and is lithostratigraphically below the Flysch zone (Figure 1). The ophiolite represents a thick slab of oceanic lithosphere, and shows a continuous sequence through oceanic lithosphere from foliated harzburgite-dunite through tranisition zone dunite, ultramafic–mafic cumulate, and gabbros to a sheeted dyke complex (Siddiqui et al., 1996; Khan et al., 2007; Kakar et al., 2014).

Based on geochemical signatures and field relations Kakar et al. (2014) proposed that this ophiolite formed in a supra-subduction zone tectonic setting in Neo-Tethys.

The Flysch zone is comprised of the Nisai and Khojak and Multana Formations which are Late Palaeocene to Pleistocene fault-bounded sedimentary successions (Maldonado et al., 2011; Kasi et al., 2012). The western fault marks the boundary between the Flysch zone and Afghan block of the Eurasian plate whereas the eastern fault boundary of the Flych zone separates it from the Indian plate (Kasi et al., 2012). The intrusions investigated in this study are found within the Nisai Formation.

The Nisai Formation is approximately 1,200 m thick and is comprised of limestone, marl and shale, with subordinate sandstone and conglomerate (Kasi et al., 2012). Qayyum (1997) has assigned a Late Palaeocene to Early Oligocene age to the Formation from foraminiferal assemblages. However, the age of the Nisai Formation in the Ziaba Gorge section, where the Nisai intrusions are found, is Middle Eocene to Early Oligocene (Aminullah, 2010; Bukhari, 2015). Variations in fossil assemblages and sedimentary units reveal that the Nisai Formation was deposited in both a shallow water carbonate platform environment, as well as in deep water slope and basin environments (Qayyum, 1997). The Oligocene Khojak formation lies conformably over the Nisai formation and a significant siliclastic input has been interpreted as a delta-fan indicating progressive shallowing of the marine environment and the final collision of India with Eurasia which, in the Early Miocene, uplifted and deformed the Nisai and Khojak formations (Qayyum, 1997; Kasi et al., 2012).

Local geology and petrography

The Nisai intrusions are located ~80 km northeast of Quetta within the Eocene Nisai Formation to the northeast of the Khanozai ophiolite (Figure 1). The Nisai Formation can be divided into

two main facies; at the base of the formation is a dark shaley zone, whereas the top is dominated by partially dolomitised limestone (Aminullah, 2010). The intrusions are mostly found in the lower part of the Ziaba gorge section (Figure 2) within the shale-dominated zone. Eocene ages of the Nisai intrusions have been inferred based on their cross-cutting relationships with the Nisai Formation and their absence in the younger Khojak Formation.

The Nisai igneous intrusions are predominantly sills, concordant with the host units and range in thicknesses from 1 to 10 m. The intrusions trend NE-SW and are located approximately 20 – 30 m apart. The host shales and muds have been intensely deformed, with sills also forming fragmented and isolated bodies (Figure 3a-b) as well as plugs with pinch and swell structures with linear contacts also found on a smaller scale, i.e., a few metres (Figure 3c). Most of the intrusions and country rocks show chilled and baked margins, respectively (Figure 3d).

The Nisai intrusions range from very fine-grained basaltic compositions to medium-coarse grained dolerites and gabbros. Basaltic samples consist of approximately 20 vol.% clinopyroxene micro-phenocrysts set within a groundmass of fine grained plagioclase, clinopyroxene, magnetite, secondary alteration minerals and devitrified glass. All samples are quite altered with the sericitisation of plagioclase and chloritisation and serpentinisation of clinopyroxene. In addition, three basaltic intrusions (Ni6, 8, 15) contain serpentinised olivine phenocrysts (~2.5 mm). Small (1mm) spherical inclusions containing carbonate may have been derived from the host carbonate lithologies, either by incorporation into the magma or may represent vesicles infilled with secondary carbonate.

Dolerite samples are fine-medium grained and have mostly holocrystalline ophitic textures. They comprise 60 vol.% sericitised plagioclase laths with augite (partially replaced by chlorite) and magnetite with secondary interstitial calcite and chlorite. Minor analcite and nepheline

have been identified in several of the samples. Quartz-carbonate veining is extensive within these samples.

Gabbroic samples Ni9, Ni11 and Ni14, are characterised by their coarse grained mineralogy and holocrystalline textures, with no sign of any layering or cumulate textures. Alteration products of serpentine have replaced olivine, while chlorite, amphibole and magnetite have partially replaced pyroxenes. Small quantities of fine- to medium-grained calcite and epidote are also found in the gabbroic samples in varying amounts.

Analytical procedures

Samples were collected for analyses from each of the major igneous units detailed above, (the broad sample locations are given on Figure 2 and detailed information on each analysed sample including field notes and latitude and longitude are given in Online Appendix 1) Following removal of weathered surfaces the samples were crushed in a steel jaw crusher and powdered using an agate Tema mill at Cardiff University. Two grams of sample powder were then heated in a porcelain crucible to 900 °C for 2 hours to determine loss on ignition. Major and trace element abundances were analysed using a JY Horiba Ultima 2 inductively coupled plasma optical emission spectrometer (ICP-OES) and a Thermo X7 series inductively coupled plasma mass spectrometer (ICP-MS) at Cardiff University, United Kingdom.

The ignited powders were prepared for analysis by fusion of 0.1 g ±0.0005 of sample with 0.4 g ±0.0005 lithium tetraborate flux in a platinum crucible on a Claisse Fluxy automated fusion system. The mixture was then dissolved in 30 ml of 10% HNO_3 and 20 ml of de-ionised water. After the sample was fully dissolved, 1 ml of 100 ppm Rh spike was added and the solution was made up to 100 ml with de-ionised water. ~20 ml of this solution was run on the ICP-OES to obtain the major element abundances. 1 ml of the solution was added to 1 ml of Tl and 8 ml of 2% HNO_3 and analysed on the ICP-MS to obtain the trace element abundances.

Accuracy and precision of the data were assessed using the international reference materials JB-1A and BIR-1 (Online Appendix 2). The full data set can be found in Table 1.

Geochemical results

Alteration and element mobility

Loss on ignition (LOI) values for the Nisai intrusions range from 0.40 – 2.31 wt.% and so are generally low, which may suggest little alteration,. However, LOI is a relatively imprecise indicator of alteration as different alteration minerals contain different proportions of water. Petrographic evidence and mineral assemblages including chlorite, epidote and serpentine provide evidence that the Nisai intrusions have experienced variable sub-solidus alteration and so potentially element remobilisation may have occurred.

High field strength elements (HFSE) and rare earth elements (REE) are generally regarded to be relatively immobile under low grades of metamorphism and alteration, including that of greenschist facies (e.g., Pearce, 1996; Hastie et al., 2007). In contrast, the large ion lithophile elements (LILE), apart from Th (e.g., Hastie et al., 2007), are relatively mobile under these conditions, as are major elements such as Na_2O and K_2O. Given the presence of carbonate in the alteration products of some of the intrusions and the elevated MgO values (up to 17 wt.%) in some of the samples, CaO and MgO values of the intrusions will also be treated with caution. Plots of HFSE and REE against Zr (which is assumed to be relatively immobile) show much more coherent trends (Figures 4-5) than that displayed by most of the major elements and LILE. The remainder of this study will therefore mostly focus on the relatively immobile HFSE and REE.

Classification

The total alkali vs. silica diagram shows that the major element geochemical compositions of the Nisai igneous intrusions range from basalts to andesites (Figure 5a). The majority of the igneous bodies plot within the alkaline series, with five samples plotting as tholeiitic. However because this diagram relies on the relatively mobile oxides of Na and K, the Nisai samples have also been plotted on the immobile element, Zr/Ti vs. Nb/Yb diagram (Figure 6b). As will be detailed below, all the samples except (Ni12) can be sub-divided into three groups on the basis of their REE contents and ratios. All of groups 1 and 2 and all but one sample of group 3 can be classified as alkali basalt on Figure 6b. Ni8, from group 3 plots in the basalt field with sample Ni12, and both are more tholeiitic in composition than the rest of the samples.

Major elements

Given the potential effect of carbonate-related (dolomitic and calcitic) alteration from the enclosing limestones, Zr has been used as a differentiation index for these intrusions rather than MgO or Mg# (Figure 4). Of all the major elements, Ti and P are widely regarded to be the most immobile during sub-solidus alteration. Group 1 intrusions generally have higher TiO_2, P_2O_5, 2.7-4.7 wt.% and 0.5-1.5 wt.% respectively, than the rest of the samples. In terms of the other major elements, Al_2O_3, Na_2O and SiO_2 in group 1 samples have a wider compositional range and extend to much lower values, than in the rest of the samples. In contrast, MgO and CaO in group 1 samples range to generally higher values than in groups 2 and 3 (Figure 4). Fe_2O_3 (t) contents are broadly similar in all the groups and range from 10.2-15.6 wt.%. Sample Ni21 has lower TiO_2, P_2O_5, and CaO than all the other samples, but for the other major elements the sample lies within the compositional range of groups 2 and 3 (Figure 4).

Trace elements

In group 1, the more compatible elements, Ni, Cr, Sc and Co generally display a broad decreasing trend with increasing Zr values (Figure 5). There is however considerable scatter in these trends and although these elements are generally regarded as immobile, some of this scatter may well be due to variable sub-solidus alteration, involving concentration/dilution of these elements, via. removal/addition of major elements. Likewise, groups 2 and 3 show no discernible trends for the compatible elements vs. Zr with both groups displaying a relatively wide compositional range (Figure 5).

Incompatible elements including Th, HFSE and the LREEs all have good positive correlations when plotted against Zr (Figure 5). Group 3 samples have a restricted compositional range at relatively low values for all these elements (e.g., Nb: 18-26 ppm and Zr: 120-145 ppm). In contrast, group 1 samples have a much wider compositional range, than Group 3, at higher elemental abundances, (e.g., Nb: 36-89 ppm and Zr: 137-308 ppm) such that there is no compositional overlap between groups 1 and 3. Group 1 seem to diverge into two trends at higher Zr contents (e.g., Figure 5). Compositionally, group 2 samples have intermediate incompatible trace element compositions between groups 1 and 3 (e.g., Nb: 29-47 ppm and Zr: 130-171ppm). With the exception of the HREE, Ni12 has the lowest incompatible trace element contents of all the sampled sills (e.g., Nb: 12 ppm and Zr: 101ppm).

All three groups of Nisai intrusions have enriched LREE and depleted HREE chondrite-normalised patterns and within each group they display broadly sub-parallel patterns (Figure 7). As Figure 7 shows, group 1 intrusions are generally the most enriched in the LREE [$(La/Nd)_{cn}$: 1.9-2.7) and are moderately depleted in the HREE [$(Sm/Yb)_{cn}$: 5.5-8.2]. Group 2 samples (Figure 7b) are on average slightly less-enriched in LREE and more depleted in HREE than group 1 [$(Sm/Yb)_{cn}$: 3.6-5.1]. In contrast, group 3 intrusions have lower $(La/Nd)_{cn}$ ratios (1.3-1.4) than the other two groups and range to slightly more depleted HREE signatures

[$(Sm/Yb)_{cn}$: 5.6-9.4]. These characteristic differences in REE element ratios, summarised on Figure 8a, have enabled the samples to be sub-divided into the three groups used in this paper. Ni12 has a less-enriched, LREE pattern and a flatter HREE signature [$(Sm/Yb)_{cn}$: 2.2] than the rest of the intrusions (Figure 7).

Unsurprisingly, primitive mantle-normalised multi element plots display the same features as chondrite-normalised diagrams (Figure 9). It is noticeable that the majority of group 1 have a negative Nb anomaly [$(Th/Nb)_{pmn}$ – 0.84-1.35] whereas all of group 3 intrusions have no Nb anomaly (Figures 8b and 9). The three group 2 samples display a wide range of $(Th/Nb)_{pmn}$ (0.64-1.43) and have both positive and negative Nb anomalies (Figure 8b). Ni12 has no negative Nb anomaly.

Another significant feature of group 1 is that most of the samples possess negative Ti anomalies as do some of the samples in groups 2 and 3 (Figure 9). As shown in Figure 8c the magnitude the of negative anomaly [as indicated by $(Gd/Ti)_{pmn}$ ratio] does not correlate with the extent of fractionation of the sample. However, the $(Gd/Ti)_{pmn}$ ratios display a good positive correlation with $(La/Nb)_{pmn}$ ratios (Figure 8d).

Discussion

In the following sections, we will first discuss and model the effects of fractional crystallisation and crustal vs. source contamination on the composition of the Nisai intrusions. Our results and mantle melt modelling will then be used to show that that the three compositional groups identified in the Nisai intrusions are ultimately derived from slightly different mantle sources.

Fractional Crystallisation

Fractional crystallisation has been modelled using the PELE program (Boudreau, 1999), a Windows platform version of the MELTS software (Ghiorso and Sack, 1995). Hydrous and anhydrous fractional crystallisation can be modelled using PELE between temperatures of ~500 – 2000^{o}C and pressures < 2 GPa.

Major element geochemical trends for primitive samples have been modelled using five different parameters (Table 2). Models 1, 3 and 4 are anhydrous at different pressures which correspond to depth; Models 2 and 5 contain 1 wt.% H_2O. All models use a quartz-fayalite-magnetite (QFM) oxygen buffer, with the composition of the residual magma being calculated at 10% crystallisation increments.

Fractional crystallisation of the group 1 and 2 Nisai intrusions was modelled using the composition of sample Ni10 as the proposed parent magma (MgO: 10.7 wt.%). The modelled major element trends are shown in Online appendix 3 although there is scatter due to alteration, it is evident that higher pressure (≥ 10 kbar), under either hydrous or anhydrous conditions (Models 4 and 5) are needed in order to model the composition of groups 1 and 2. Model 5 (1 wt.% H_2O) at 10 kbar predicts that crystallisation commences at ~1300°C with olivine being the first to crystallise, followed successively by clinopyroxene, spinel and plagioclase.

Ni7, one of the least-petrographically altered samples, was used as the parental magma of group 3 igneous intrusions (MgO: 9.28 wt.%). As shown in the Electronic appendix, the major element trends of group 3 are better explained using hydrous models (1 wt.% H_2O). Overall, Model 5 (10 kbar and 1 wt.% H_2O) provides the best fit to the data. This model predicts that crystallisation begins at ~1300°C with olivine being the first mineral to crystallise followed successively by clinopyroxene, spinel, orthopyroxene and plagioclase.

Using immobile trace elements (e.g., Zr, Th and Nb) as opposed to major elements to model this fractional crystallisation (Figure 10) yields results that are slightly clearer and suggest that model 5 (10 kbar and 1 wt.% H_2O) broadly fits both groups 1 and 3, with group 2 plotting between the modelled trends for groups 1 and 3. This modelling suggests that groups 2 and 3 underwent < 20% fractional crystallisation, whereas group 1 samples have compositions consistent with up to 50% fractional crystallisation.

Crustal assimilation vs. subduction input

Although fractional crystallisation modelling can replicate the compositions of the Nisai intrusions reasonably well, given the fact that most of group 1 and one sample from group 2 have elevated Th contents and negative Nb anomalies (Figure 9) the potential role of crustal contamination and/or an input from a subduction zone also needs to be assessed.

Assimilation fractional crystallisation (AFC) modelling has been carried out using trace element concentrations calculated by PELE and standard AFC equations (DePaolo, 1981) using a ratio of assimilation/crystallisation (*r*) ranging from 0.1 to 0.6. The composition of average felsic crust (a more likely assimilant than bulk crust) from Rudnick and Gao (2003) has been used as a contaminant.

Although, AFC modelling using Ni7 as the parental magma, at pressures of 10 kbar with 1 wt.% H_2O (established from fractional crystallisation modelling) can explain both the negative Nb and positive Th anomalies on primitive mantle normalised diagrams, this however requires an *r* value (mass ratio of assimilation to crystallization) of up to 0.6 (Figure 10c), which may be unrealistic. The main reason why such a large amount of crust is needed to replicate the trace element composition of samples with Nb depletion, is because Ni7 has a positive Nb anomaly and this, given the fact that the magmas also appear to be hydrous, combined with a good

positive correlation between the magnitude of the negative Nb and Ti anomalies (Figure 8d), suggests that a subduction input to the source of the magmas might be a more reasonable model. A subduction-related origin for these Nb and Ti anomalies is also apparently confirmed by the presence of negative Zr anomalies [$(Sm/Zr)_{pmn} > 1$] (Figure 9) strongly implying the influence of fluids derived from a slab containing residual rutile (Foley et al., 2000).

Mantle melt modelling

Pooled fractional melt calculations have been used to model the composition (depleted vs primitive mantle) and mineralogy (lherzolite containing either spinel or garnet or a 50:50 mix representing melting across the transition zone) of the source region. Partition coefficients are averages from Salters and Longhi (1999), Salters et al. (2002) and McDade et al. (2003). Mantle mineral proportions and source compositions have been taken from (McKenzie and O'Nions, 1991). The results of the modelling are summarised on Figure 11.

Models which use a more-enriched (primitive) mantle source are a much better fit to the compositional data of all the samples in this study. Samples in group 3 are consistently slightly more depleted in LREE relative to groups 1 and 2. The modelling suggests that the lower $(La/Nd)_{cn}$ ratios in group 3 are consistent with a slightly more depleted source region (Figure 11).

As expected from their steep REE patterns all sample groups are derived from a source containing garnet. However the garnet control varies between the different groups, and appears to be slightly more significant for group 3 samples, with groups 1 and 2 being derived from a shallower source region encompassing more of the spinel-garnet transition zone (Figure 11). Group 2 samples all plot below the 50:50 garnet-spinel melt model curve, suggesting a shallower source than group 1 and this is consistent with the higher degrees of mantle melting

(2–5%) required to replicate the compositions of group 2. In contrast, groups 1 and 3 are best modelled by lower degrees of melting (1-2% and ~1% respectively). Ni12 appears to be the result of much more extensive (15-20%) and shallower melting, with a relatively small proportion of garnet lherzolite in the source.

Mantle sources

Several constraints on the mantle source region have already been outlined in the preceding discussion. It has been ascertained that the source region contained a subduction-related component and was enriched. The enriched nature of the samples is confirmed by a Ti vs. V plot on which most of the samples have compositions consistent with an enriched ocean island basalt (OIB)-like source region (Figure 12a). However, samples Ni12 and group 2 samples, trend towards and, plot in the back arc basin (BAB) and mid-ocean ridge (MORB) field and so lend support to a subduction influence in these basalts.

The OIB-like nature of the intrusions is also evident on a Nb/Yb vs. Th/Yb plot (Pearce, 2008) with about half of the samples plotting within the MORB-OIB array. The remainder of the samples plot above this array (Figure 12b). Most of the samples in groups 1 and 2 plot slightly above the MORB-OIB array and this might be due to either crustal contamination or a subduction influence, (Pearce, 2008) but given the evidence presented above, a subduction influence seems more likely. The enriched nature of these intrusions is one of the reasons why a subduction influence is relatively difficult to identify. Sample Ni12 plots more towards the depleted end of the MORB-OIB array on Figure 12b. Although work presented by Li et al (2015) has recently outlined some problems relating to the indiscriminate use of incompatible trace element ratios for tectonic discrimination purposes, the point made by these authors is that such diagrams should not be used in isolation as the sole line of evidence for the tectonic setting of a suite of rocks. The evidence from this Nb/Yb vs. Th/Yb plot is consistent with both

other geochemical evidence (in particular multi-element normalised diagrams) presented herein, and the regional tectonic setting.

Pearce (2008) noted that higher degrees of melting resulting from lower melting temperatures caused by volatiles would mean that subduction influenced samples would plot in the MORB field on a TiO_2/Yb vs. Nb/Yb diagram (Figure 12c). Group 1 samples trend vertically towards the MORB field, although they do not plot within it on Figure 12c). This trend is due to their negative Ti anomalies, and provides further evidence for a subduction influence in the mantle source region.

The subduction input to the Nisai intrusions is unsurprising, given that around this time the Indian plate collided with the Eurasian plate: a process that was facilitated by the subduction of Tethyan oceanic crust below the region from ca. 100 Ma (e.g., Bignold et al., 2006; Khan et al., 2009). A reduced rate of convergence in the Eocene as the collision entered its final phase is likely to have resulted in oceanic slab detachment (cf. Davies and Von Blanckenburg, 1995). Upwelling and decompression of deep asthenosphere through the ensuing slab tear and its interaction with subduction-modified mantle may have led to the formation of the enriched OIB-type melt with a subduction signature required to form the Nisai intrusions (Figure 13).

Similar slab detachment models along with upwelling and decompression melting of deep asthenosphere have also been proposed as the cause of Eocene-age post-collisional magmatism found in several other locations along the Neo-Tethyan suture zone. Such Eocene volcanic and intrusive sequences have been particularly well-documented in eastern Anatolia-northern Iran-Azerbaijan (Dilek et al., 2010), western Anatolia (Altunkaynak and Dilek, 2006), northern Anatolia (Keskin et al., 2008) and also in the Gaoligong–Tengliang belt, eastern Tibet (Xu et al., 2008). The available geochemical data from these areas has been plotted on Figures 6, 8

and 12, for comparison with the compositional data from the Nisai intrusions. The most striking thing about the data, both from Anatolia and Tibet is that it is all generally less-enriched, more tholeiitic and more MORB-like than the alkaline and OIB-like Nisai intrusions. In terms of post-collisional Eocene magmatism in the Neotethyan suture zone the Nisai intrusions are therefore unique.

The enriched OIB-like nature of the mantle source of the Nisai intrusions rather than depleted upper (MORB-source) mantle is suggestive of a mantle plume source region. Cretaceous (~70 Ma) alkaline sills and lavas in the Muslim Bagh-Khanozai region, (Mahoney et al. 2002 and Kerr et al., 2010) have been interpreted as some of the earliest melts from the Réunion hotspot, the plume head phase of which also formed the Deccan Traps at ~65 Ma (Hooper et al., 2010). The Nisai intrusions are only a few kilometres from these sills (Figure 2) and although the time gap between these two sets of intrusive rocks is ~20 myr, they have similar geochemical signatures (Figure 8a-b) and both are the result of relatively low degrees (<5%) of melting of similar enriched garnet-bearing mantle sources (Kerr et al., 2010). Furthermore, any small scale localised extension during the India-Eurasia collision would have facilitated both decompression melting of the asthenosphere and provided a lithospheric weak zone along which the melts could ascend towards the surface. Based on magmatism in south-central Anatolia, Dilek and Whitney (2000) have invoked a similar mechanism to explain the ascent of post-collisional slab break-off magmas through the lithosphere via brittle-ductile faults and shear zones.

Although the Cretaceous alkaline sills are ~20 myr older than the Nisai intrusions residual mantle material from a plume head can remain thermally buoyant and retain its geochemical signature for at least 200 myr (Campbell, 2007). Due to this buoyancy the residual plume head mantle can move with the overlying lithosphere (Griffiths and Campbell, 1990). Significantly,

these predicted thermal anomalies have been detected below the Deccan flood basalt province (Kennett and Widiyantoro, 1999). It is therefore possible that residual Réunion plume material may have played a significant role in the formation of the Nisai intrusions.

Concluding tectonomagmatic model

Based on the preceding discussion, the following tectonomagmatic model (Figure 13) for the formation of the Nisai intrusions can be constructed:

1. The Eocene Nisai shales and limestones were deposited (*ca.* 55 – 35 Ma) on the oceanic crust of the Eurasian plate. This oceanic crust was formed by extensional tectonism (*ca.* 90 – 80 Ma) in the Neo-Tethyan ocean basin.

2. Slab fluid release and slab detachment coincided with localised extension to facilitate decompression asthenospheric melting which may have been aided by residual (warmer) asthenosphere from the Réunion plume. This resulted in melting of a more-enriched mantle source over a range of (garnet-bearing) depths within a melt column leading to the formation of enriched OIB-like melts (Fig. 6.24). The discovery of a less-enriched intrusion (Ni12) suggests that in places the residual plume material also mixed with ambient upper mantle.

3. Melt produced within the asthenosphere (> 60-80 km), rose through the asthenosphere and percolated through the lithosphere via brittle-ductile faults and shear zones perhaps resulting from localised extension of the Eurasian plate (cf. Dilek and Whitney, 2000). The hydrous melt pooled and fractionated within a magma chamber in the crustally thickened lithosphere (perhaps with a small amount of crustal assimilation) at

approximately 30 km (10 kbar) and was intermittently tapped resulting in the upward migration of melt and subsequent intrusion of the Nisai sills.

4. Continued collision of Indian and Eurasian plates within this crustal thickening zone obducted the Khanozai and Muslim Bagh ophiolites and the rest of the suture zone and uplifted the Nisai formation and intrusions along with the overlying Kojack formation. The main driving force for the regional uplift along the suture zone may well have been isostatic rebound and uplift of the partially subducted Indian continental margin. This phenomenon has also been well-documented in Anatolia (Dilek and Whitney, 2000; Dilek et al., 2010;) following the latest Cretaceous-Tertiary continental subduction events.

Acknowledgements

Aminullah and Wajid from the University of Balochistan, Quetta are thanked for their help during fieldwork and sample collection. Comments by Alan Hastie on an early draft of this paper are appreciated.

References

Altunkaynak, S, and Dilek, Y. 2006. Timing and nature of postcollisional volcanism in western Anatolia and geodynamic implications. In Dilek, Y., and Pavlides, S. (eds.) Postcollisional tectonics and magmatism in the Mediterranean region and Asia. Geological Society of America Special Paper 409, 321–351

Aminullah, 2010. Sedimentology and Petrology of the Nisai Formation, Pishin Basin, Muslim Bagh-Khanozai area, Balochistan, Pakistan. Unpublished M.Phil. Thesis, University of Balochistan. 96p.

Asrarullah, Z. A., and Abbas, S. G., 1979. Ophiolites in Pakistan: an introduction. Geodynamics of Pakistan. Geological Survey of Pakistan, Quetta, 181-192.

Bannert, D., Cheema, A., Ahmed, A. and Schaefer, U. 1992. The structural development of the western fold belt, Pakistan. Geologisches Jahrbuch Reihe B Regionale Geologie Ausland, 80, 3-60.

Beck, R.A., Burbank, D.W., Sercombe, W.J., Riley, G.W., Barndt, J.K., Berry, J.R., Afzal, J., Khan, M.A., Jurgen, H., Metje, J., Cheema, A., Shafique, N.A., Lawrence, R.D., Khan, M.A., 1995.Stratigraphic evidence for an early collision between northwest India and Asia. Nature 373, 55–58.

Besse, J., Courtillot, V., Pozzi, J.P., Westphal, M. and Zhou, Y.X., 1984. Palaeomagneric estimates of crustal shortening in the Himalayan thrusts and Zangbo suture. Nature, 311, 621-626.

Bignold, S.M., Treloar, P.J. and Petford, N., 2006. Changing sources of magma generation beneath intra-oceanic island arcs: An insight from the juvenile Kohistan island arc, Pakistan Himalaya. Chemical Geology, 233, 46-74.

Boudreau, A.E., 1999. PELE-a version of the MELTS software program for the PC platform. Computers and Geoscience, 201-203, 25, 201-203.

Bouilhol, P., Jagoutz, O., Hanchar, J.M. and Dudas, F.O., 2013. Dating the India-Eurasian collision through arc magmatic records. Earth and Planetary Science Letters, 366, 163-175.

Bukhari, S.W.H., 2015. Larger benthic foraminiferal biostratigraphy of the Nisai Formation, Pishin Belt, Balochistan, Pakistan. Unpublished M.S. Thesis, Centre of Excellence in Mineralogy, University of Balochistan, Quetta. 60p.

Campbell, I.H., 2007. Testing the plume theory. Chemical Geology, 241, 153-176.

Davies, J.W. and Von Blanckenburg, F., 1995. Slab breakoff: a model of lithosphere detachment and its test in the magmatism and deformation of collisional orogens. Earth and Planetary Science Letters, 129, 85-102.

DePaolo, D.J., 1981. Trace element and isotopic effects of combined wallrock assimilation and fractional crystallization. Earth and Planetary Science Letters, 53, 189-202.

Dilek, Y. and Furnes, H., 2009. Structure and geochemistry of Tethyan ophiolites and their petrogenesis in subduction rollback systems. Lithos, 113, 1-20.

Dilek, Y., Imamverdiyev, N. and Altunkaynak, S. 2010. Geochemistry and tectonics of Cenozoic volcanism in the LesserCaucasus (Azerbaijan) and the peri-Arabian region: collision-induced mantle dynamics and its magmatic fingerprint. International Geology Review, 2, 536–578.

Dilek, Y., and Whitney, D.L. 2000 Cenozoic crustal evolution in central Anatolia: extension, magmatism, and landscape development. In: Panayides, I., Xenophontos, C., and Malpas, J. (eds). Proceedings of the Third International Conference on the Geology of the Eastern Mediterranean. Geological Survey Department, Nicosia, Cyprus, 183-192.

Durrani, R.A.M., Kassi, A.M. and Kassi, A.K. 2012. Petrology and provenance of the sandstone channel succession within the Jurassic Loralai Formation, Sulaiman Fold-Thrust Belt, Pakistan. Journal of Himalayan Earth Sciences, 45(1), 1-16.

Foley, S.F., Barth, M.G. and Jenner, G., 2000. Rutile/melt partition coefficients for trace elements and an assessment of the influence of rutile on the trace element characteristics of subduction zone magmas. Geochimica et Cosmochimica Acta, 64, 933-938.

Ghiorso, M.S. and Sack, R.O., 1995. Chemical mass transfer in magmatic processes .4. A revised and internally consistent thermodynamic model for the interpolation and extrapolation of liquid solid equilibria in magmatic systems at elevated temperatures and pressures. Contributions to Mineralogy and Petrology, 119, 197-212.

Gnos, E., Immenhauser, A. and Peters, T., 1997. Late Cretaceous/early Tertiary convergence between the Indian and Arabian plates recorded in ophiolites and related sediments. Tectonophysics, 271, 1-19.

Griffiths, R.W. and Campbell, I.H., 1990. On the dynamics of long-lived plume conduits in the convecting mantle. Earth and Planetary Science Letters, 103, 214-227.

Hastie, A.R., Kerr, A.C., Pearce, J.A. and Mitchell, S.F. 2007. Classification of altered volcanic island arc rocks using immobile trace elements: Development of the Co-Th discrimination diagram. Journal of Petrology, 48, 2341-2357.

Hooper, P., Widdowson, M. and Kelley, S., 2010. Tectonic setting and timing of the final Deccan flood basalt eruptions. 38, 839-842.

Hunting Survey Corporation Ltd. 1960. Reconnaissance geology of part of Western Pakistan. A Columbo Plan Cooperative Project (a report published for the government of Pakistan by the Government of Canada), Toronto.

Jaeger, J.-J., Courtillot, V. and Taponnier, P., 1989. Paleontological view of the ages of the Deccan Traps, the Cretaceous-Tertiary boundary, and the India-Asia collision. Geology, 18, 316-319.

Kakar, M.I., Collins, A.S., Mahmood, K., Foden, J.D. and Khan, M., 2012. U-Pb zircon crystallization age of the Muslim Bagh ophiolite: Enigmatic remains of an extensive pre-Himalayan arc. Geology, 40, 1099-1102.

Kakar, M.I., Kerr, A.C., Mahmood, K., Collins, A.S., Khan, M. and McDonald, I., 2014. Supra-subduction zone tectonic setting of the Muslim Bagh Ophiolite, northwestern Pakistan: Insights from geochemistry and petrology. Lithos, 202-203, 190-206.

Kasi, A.K., Kassi, A.M., Umar, M., Manan, R.A. and Kakar, M.I., 2012. Revised Lithostratigraphy of the Pishin Belt, northwestern Pakistan. Journal of Himalayan Earth Sciences, 45, 53-65.

Kennett, B.L.N. and Widiyantoro, S., 1999. A low seismic wavespeed anomaly beneath northwestern India: a seismic signature of the Deccan plume? Earth and Planetary Science Letters, 165 145-155.

Kerr, A.C., Khan, M., Mahoney, J.J., Nicholson, K.N. and Hall, C.M., 2010. Late Cretaceous alkaline sills of the south Tethyan suture zone, Pakistan: Initial melts of the Réunion hotspot? Lithos, 117, 161-171.

Keskin, M., Can Genç, S. and Tüysüz, O. 2008. Petrology and geochemistry of post-collisional Middle Eocene volcanic units in North-Central Turkey: Evidence for magma generation by slab breakoff following the closure of the Northern Neotethys Ocean. Lithos, 104, 267–305.

Khan, M., Kerr, A.C. and Mahmood, K., 2007. Formation and tectonic evolution of the Cretaceous-Jurassic Muslim Bagh ophiolitic complex, Pakistan: Implications for the composite tectonic setting of ophiolites. Journal of Asian Earth Sciences, 31, 112-127.

Le Maitre, R.W. 2002. Igneous Rocks: A Classification and Glossary of Terms. Cambridge University Press, Cambridge, UK.

Li, C., Arndt, N.T., Tang, Q. and Ripley, E.M., 2015. Trace element indiscrimination diagrams. Lithos, 232: 76-83.

Khan, S. D., Walker, D. J., Hall, S. A., Burke, K. C., Shah, M. T., & Stockli, L. (2009). Did the Kohistan-Ladakh island arc collide first with India? Geological Society of America Bulletin, 121(3-4), 366-384.

Mahmood, K., Boudier, F., Gnos, E., Monie, P. and Nicolas, A., 1995. Ar-40/Ar-39 Dating of the Emplacement of the Muslim-Bagh Ophiolite, Pakistan. Tectonophysics, 250, 169-181.

Mahoney, J.J., Duncan, R.A., Khan, W., Gnos, E. and McCormick, G.R., 2002. Cretaceous volcanic rocks of the South Tethyan suture zone, Pakistan: implications for the Reunion hotspot and Deccan Traps. Earth and Planetary Science Letters, 203, 295-310.

Maldonado, F., Mengal, J.M., Khan, S.H. and Warwick, P.D., 2011. Summary of the stratigraphy and structural elements related to plate convergence of the Quetta-Muslim Bagh-Sibi region, Balochistan, west-central Pakistan. United States Geological Survey Open-File Report, Boulder, Colorado, 2011–1224, 19 p.

McDade, P., Blundy, J.D. and Wood, B.J., 2003. Trace element partitioning on the Tinaquillo lherzolite solidus at 1.5 GPa Physics of the Earth and Planetary Interiors, 139, 129-147.

McKenzie, D. and O'Nions, R.K., 1991. Partial melt distributions from inversion of rare earth element concentrations. Journal of Petrology, 32, 1021-1091.

Mengal, J.M., Kimura, K., Siddiqui, M.R.H., Kojima, S., Naka, T., Bakht, M.S. and Kamada, K., 1994. The lithology and structure of a Mesozoic sedimentary-igneous assemblage beneath the Muslim Bagh Ophiolite, northern Balochistan, Pakistan. Bulletin of the Geological Survey of Japan, 45, 51-61.

Miyashiro, A. 1978. Nature of alkalic volcanic rock series. Contributions to Mineralogy and Petrology, 66, 91104.

Pearce, J.A., 1996. A user's guide to basalt discrimination diagrams. In: D.A. Wyman (Editor), Trace Element Geochemistry of Volcanic Rocks: Applications for Massive Sulphide Exploration, Geological Association of Canada, Short Course Notes, 12, 79-113.

Pearce, J.A., 2008. Geochemical fingerprinting of oceanic basalts with applications to ophiolite classification and the search for Archean oceanic crust. Lithos, 100, 14-48.

Peters, T., 2000. Formation and evolution of the western Indian Ocean as evidenced by the Masirah Ophiolite: A review. Geological Society of America Special Paper, 349, 525-536.

Plummer, P.S., 1996. The Amirante ridge/ trough complex: response to rotational Transform rift/ drift between Seychelles and Madagascar. Terra. Nova, 8, 34-47.

Qayyum, M., 1997. Sedimentation and tectonics in the Tertiary Katawaz Basin, NW Pakistan: A basin analysis approach, Unpublished thesis (PhD), Corvallis, Oregon State University, 480 p.

Rudnick, R.L. and Gao, S., 2003. Composition of the continental crust, In: Volume 3: The Crust p. 1-64 (Ed R.L. Rudinck) Vol. 3 Treatise on Geochemistry (eds. Holland, Holland, H.G., Turekian, K.K.) Elsevier-Pergamon, Oxford.

Salters, V.J.M. and Longhi, J., 1999. Trace element partitioning during the initial stages of melting beneath mid-ocean ridges. Earth and Planetary Science Letters, 166, 15-30.

Salters, V.J.M., Longhi, J.E. and Bizimis, M., 2002. Near mantle solidus trace element partitioning at pressures up to 3.4 GPa. Geochemistry Geophysics Geosystems. 3, doi: 10.1029/2001GC000148.

Shervais, J.W. 1982. Ti-V plots and the petrogenesis of modern ophiolitic lavas. Earth and Planetary Science Letters, 59, 101-118.

Siddiqui, R.H., Aziz, A., Mengal, J.M., Hoshino, K. and Sawada, Y., 1996. Geology, petrochemistry and tectonic evolution of Muslim Bagh Ophiolite Complex Balochistan.

Pakistan Geologica, Geoscience Laboratory, Geological Survey Pakistan, Islamabad, 3, 11-46.

Sun, S.-s. and McDonough, W.F., 1989. Chemical and isotope systematics of oceanic basalts: implications for mantle composition and processes. In: A.D. Saunders and M.J. Norry (Editors), Magmatism in the Ocean Basins. Geological Society of London, Special Publication, pp. 313-345.

Warraich, M.Y., Ali, M., Ahmad, M.N., Siddiqui, R.H. and Hirayama, J., 1995. Geology and Structure of the Calcareous Zone in Muslim Bagh and Kila Saifullah Area. Balochistan. Geoscience Laboratory Project, 1, 61-75.

Xu, Y-G., Lan, Y-B., Yang, Q-J., Huang, X-L. and Qiu, H-N. 2008. Eocene break-off of the Neo-Tethyan slab as inferred from intraplate-type mafic dykes in the Gaoligong orogenic belt, eastern Tibet. Chemical Geology, 255, 439–453.

Figure captions

Figure 1. Geological map of north-western Balochistan, Pakistan showing the Muslim Bagh-Khanozai ophiolite and the sedimentary formations discussed in the text. The location of Figure 2 is also indicated. Map modified from Bannert et al. (1992).

Figure 2. Geological sketch map of the Khanozai area northwestern Balochistan showing the Nisai Formation, the studied intrusions and sample locations in the Ziaba Gorge. Map modified from Hunting Survey Corporation (1960)

Figure 3. a-b) Isolated and fragmented bodies of sills within the Ziaba gorge; c) A close-up view of the chilled margin of a sill cutting through shale: d) Baked shale at the margin of a large sill near Ziaba gorge.

Figure 4 Representative variation diagrams of major element compositions vs. Zr for the Nisai intrusions.

Figure 5 Representative variation diagrams of trace element compositions vs. Zr for the Nisai intrusions.

Figure 6. Classification diagrams for the Nisai intrusions a) total alkali silica classification diagram (Le Maitre, 2002); tholeiitic-alkalic divide from Miyashiro,1978; (b) Zr/Ti vs. Nb/Y classification diagram (Pearce, 1996). Compositional fields for similar Eocene volcanics and intrusions from northern Anatolia (NA), western Anatolia (WA) and eastern Tibet (ET) are also shown. Data sources: EA - Keskin et al. (2008); WA - Altunkaynak and Dilek (2006); and ET - Xu et al. (2008)., northern Anatolia (Keskin et al., 2008).

Figure 7 Chondrite normalised (Sun and McDonough, 1989) rare earth element patterns for the three groups of the Nisai intrusions. Each diagram shows the samples from one group along with compositional fields for the other two groups along with Ni12.

Figure 8 Incompatible trace element ratio:ratio plots a) $(Sm/Yb)_{cn}$ vs. $(La/Nd)_{cn}$; b) $(Th/Nb)_{pmn}$ vs. $(La/Nb)_{pmn}$; c) $(Gd/Ti)_{pmn}$ vs. Zr d) $(Gd/Ti)_{pmn}$ vs $(La/Nb)_{pmn}$.The Cretaceous ultramafic lamprophyre and alkali dolerite data is from Kerr et al. 2010). Compositional fields for Eocene volcanics and intrusions from northern Anatolia (NA), western Anatolia (WA) and eastern Tibet (ET) are also shown. Data sources: see Figure 6.

Figure 9 Primitive mantle normalised (Sun and McDonough, 1989) trace element patterns for the three groups of the Nisai intrusions. Each diagram shows the samples from one group along with compositional fields for the other two groups along with Ni12.

Figure 10 a, b. Plots of Th and Nb vs. Zr for the Nisai intrusions showing modelled fractional crystallisation trends using Ni10 (group 1) and Ni7 (group 3) as starting compositions. Markers on the modelled curves are placed at 10% crystallisation intervals. Figure 10c. Plot of Nb/Nb* vs. Zr showing modelled fractional crystallization and assimilation-fractional crystallization trends for a range of r (rate of assimilation/rate of fractional crystallization) values using a starting composition of Ni7. Markers are

placed at 10% crystallisation intervals. Nb/Nb* is calculated using the following equation: $Nb_{pmn}/((Th_{pmn}+La_{pmn})/2)$. See text for more details.

Figure 11 Modelling results from pooled fractional melting calculations for various mantle source regions. Numbered ticks on the melting curves indicate percentage of partial melting. Abbreviations: Gt – garnet; Sp – spinel; lz – lherzolite; PM – primitive mantle; DM – depleted mantle. See text for details of source compositions, partition coefficients and other modelling parameters.

Figure 12 a) Plots of Ti/1000 vs. V (from Shervais, 1982); b) Th/Yb vs. Nb/Yb (from Pearce, 2008); **c)** TiO_2/Yb vs. Nb/Y (from Pearce, 2008). Compositional fields for Eocene volcanics and intrusions from northern Anatolia (NA), western Anatolia (WA) and eastern Tibet (ET) are also shown. Data sources: see Figure 6.

Figure 13 Schematic tectonomagmatic model for the formation of the Nisai intrusions (not to scale). See text for further discussion.

Tables

Table 1. Representative data set of major and trace elements

Table 2. Parameters used to model fractional crystallisation of the Nisai igneous intrusions.

Online appendices

Online appendix 1. Detailed sample locations and field notes

Online appendix 2. Replicate analysis of standards

Online appendix 3. Fractional crystallisation modelling

Figure 1

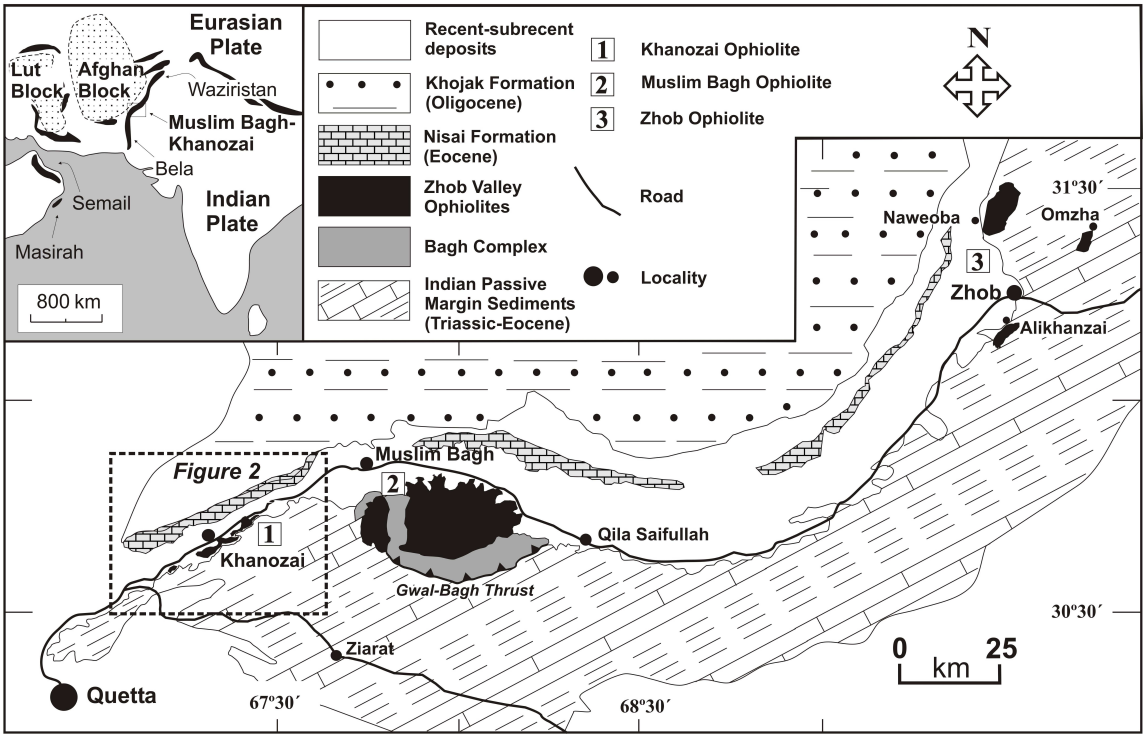
Eurasian Plate
Lut Block
Afghan Block
Waziristan
Muslim Bagh-Khanozai
Bela
Semail
Indian Plate
Masirah
800 km
Recent-subrecent deposits
Khojak Formation (Oligocene)
Nisai Formation (Eocene)
Zhob Valley Ophiolites
Bagh Complex
Indian Passive Margin Sediments (Triassic-Eocene)
1 Khanozai Ophiolite
2 Muslim Bagh Ophiolite
3 Zhob Ophiolite
Road
Locality
N
31°30′
Naweoba
Omzha
3
Zhob
Alikhanzai
Figure 2
Muslim Bagh
2
1
Khanozai
Qila Saifullah
Gwal-Bagh Thrust
30°30′
Ziarat
Quetta
67°30′
68°30′
0 25
km

Figure 2

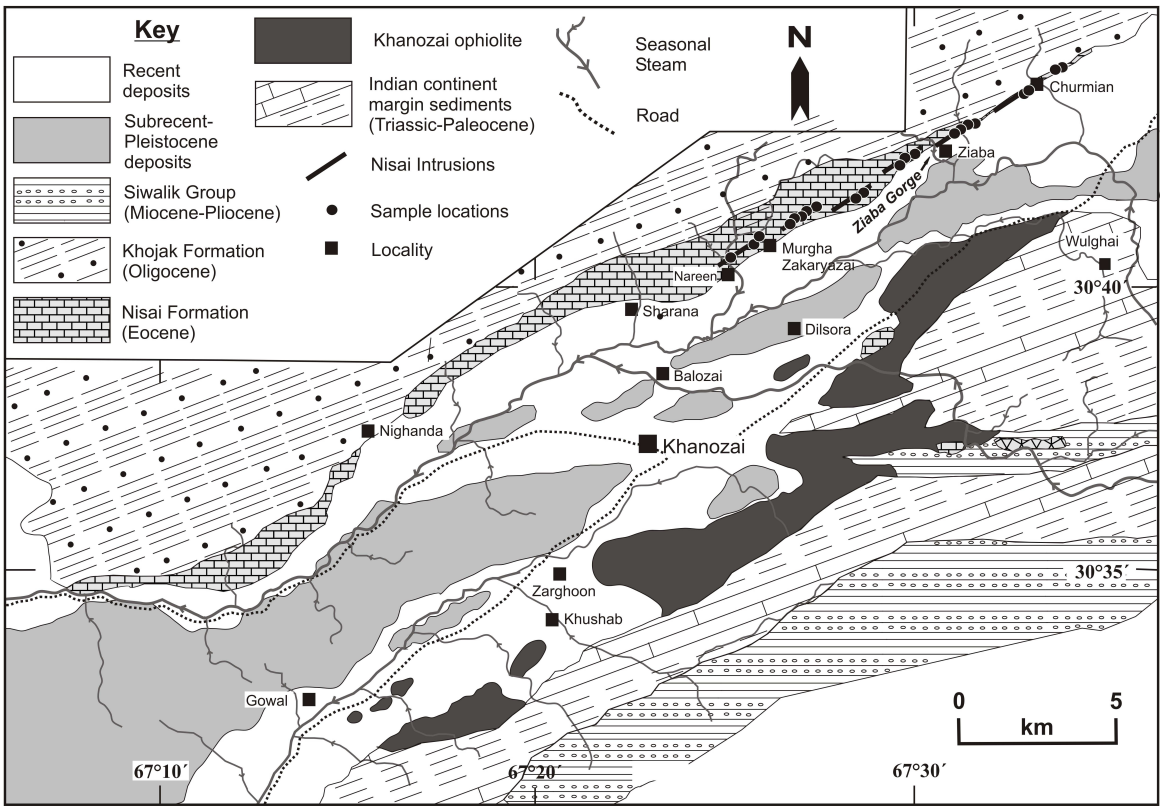
Key
Recent deposits
Subrecent-Pleistocene deposits
Siwalik Group (Miocene-Pliocene)
Khojak Formation (Oligocene)
Nisai Formation (Eocene)
Khanozai ophiolite
Indian continent margin sediments (Triassic-Paleocene)
Nisai Intrusions
Sample locations
Locality
Seasonal Steam
Road
N
Churmian
Ziaba
Ziaba Gorge
Murgha Zakaryazai
Nareen
Sharana
Dilsora
Balozai
Wulghai
30°40´
Nighanda
Khanozai
Zarghoon
Khushab
30°35´
Gowal
0
5
km
67°10´
67°20´
67°30´

FIGURE 3

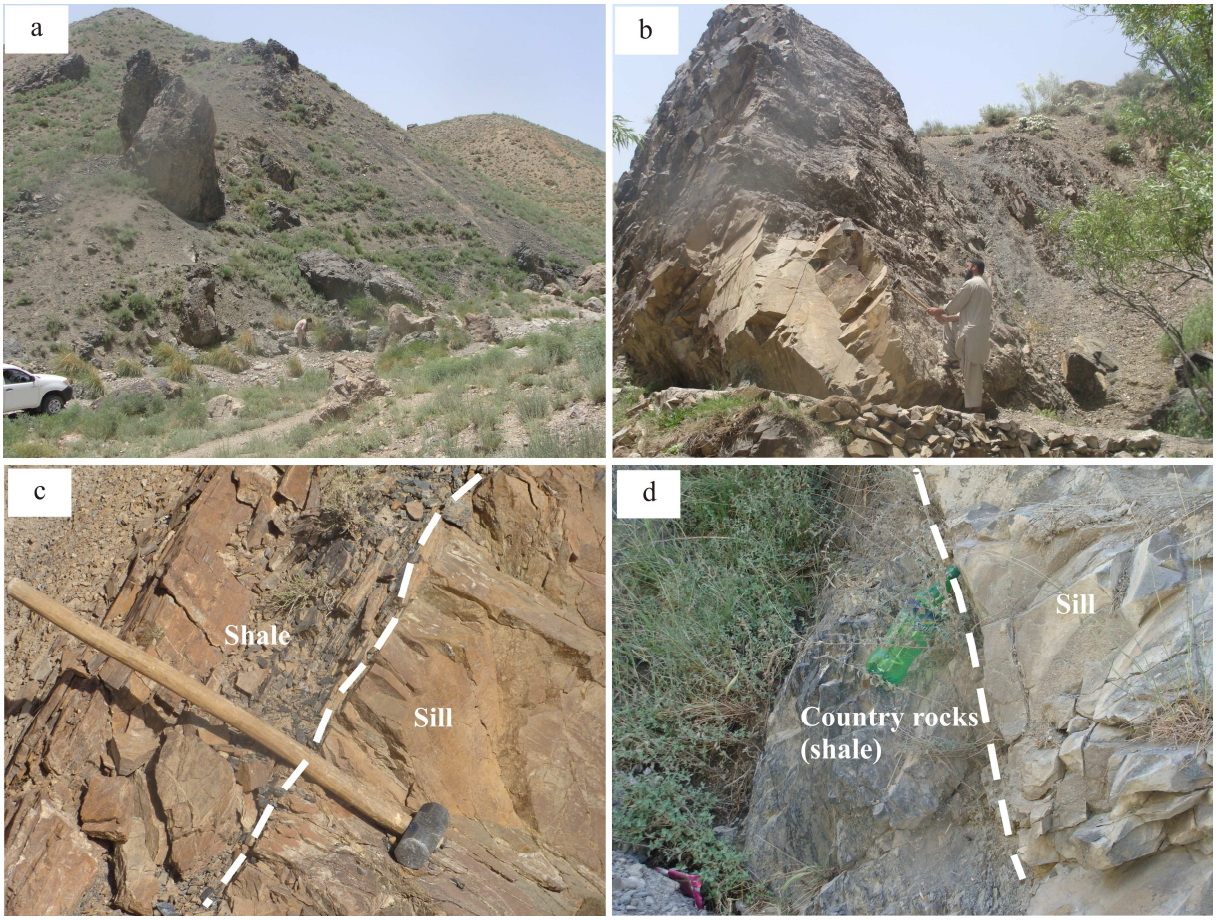

Figure 4

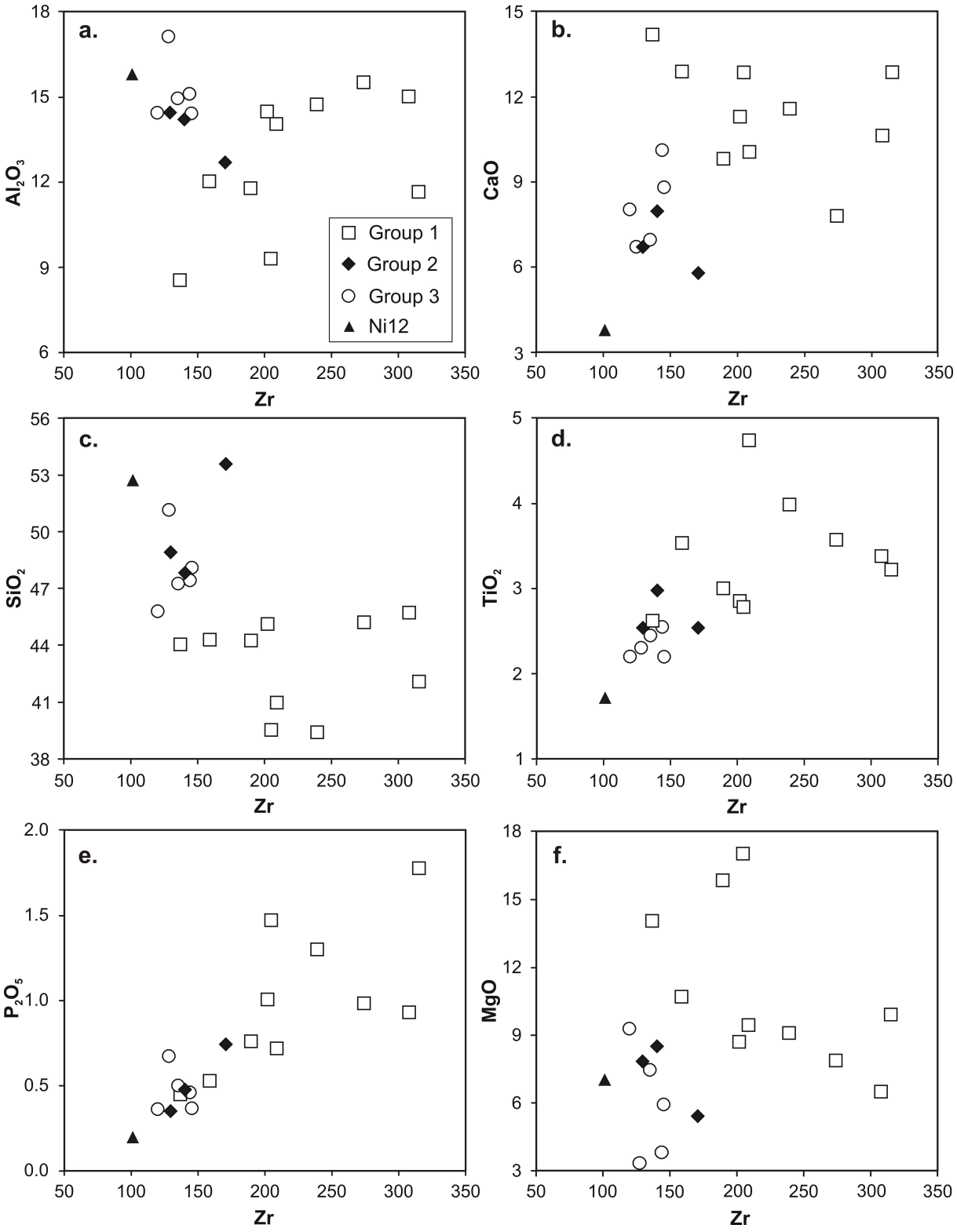
a.
b.
c.
d.
e.
f.
Al2O3
CaO
SiO2
TiO2
P2O5
MgO
Zr
Group 1
Group 2
Group 3
Ni12

Figure 5

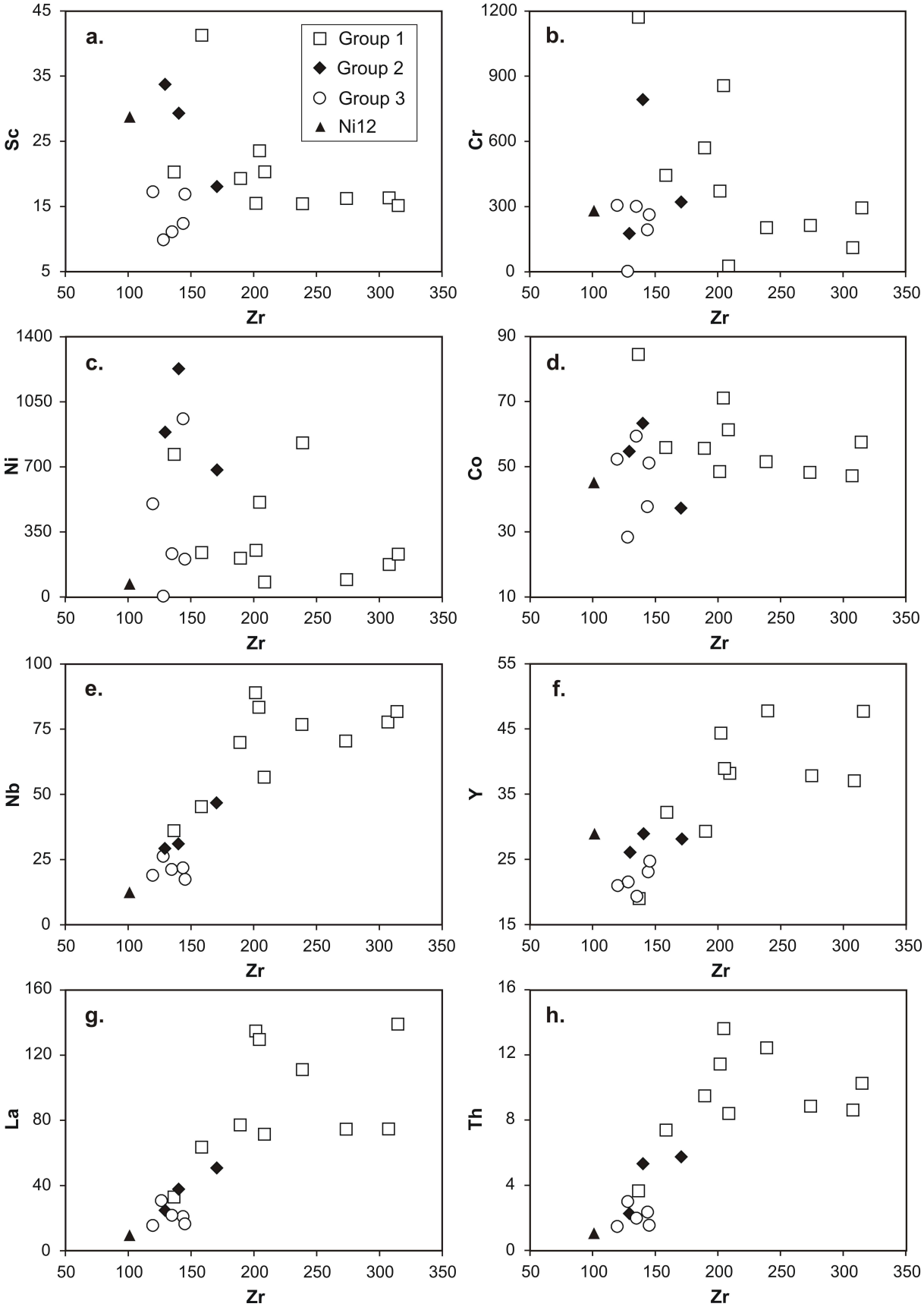
a.
Group 1
Group 2
Group 3
Ni12
Sc
Zr
b.
Cr
Zr
c.
Ni
Zr
d.
Co
Zr
e.
Nb
Zr
f.
Y
Zr
g.
La
Zr
h.
Th
Zr

Figure 6

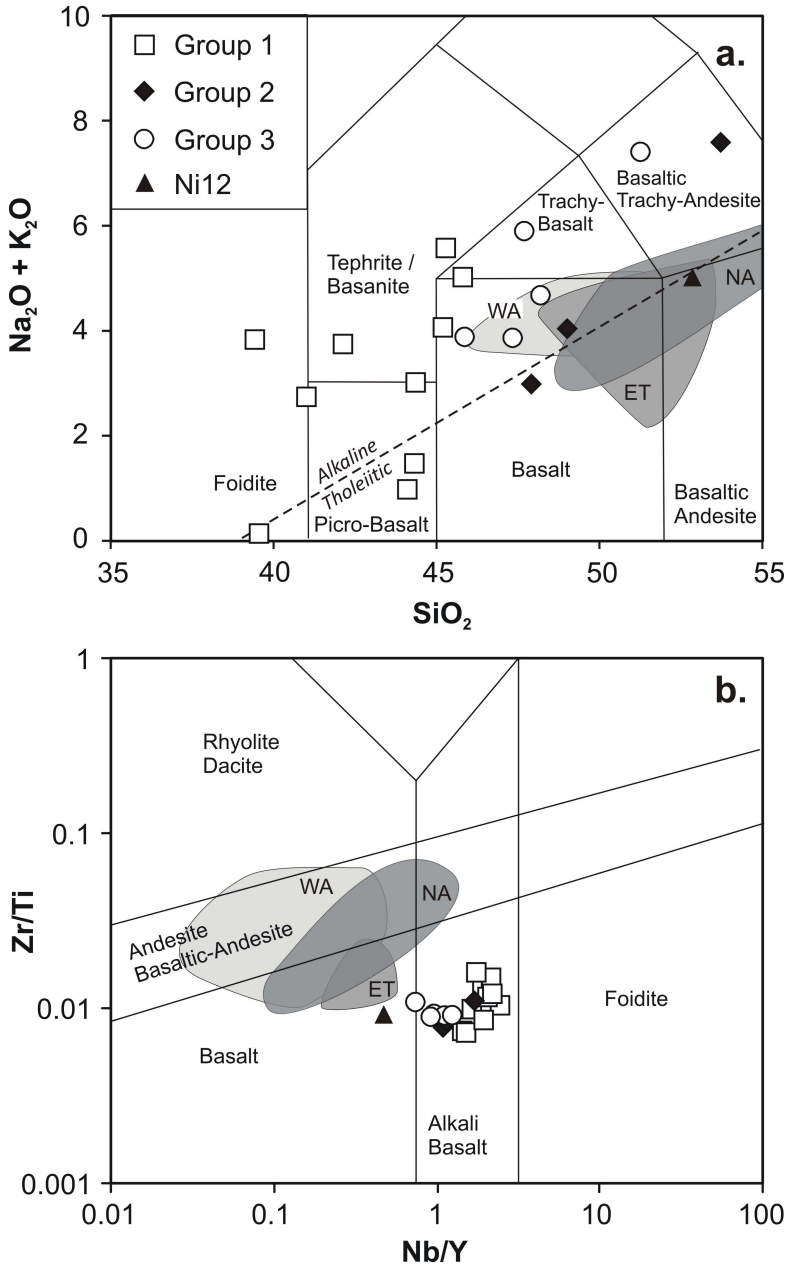
a.
Group 1
Group 2
Group 3
Ni12
Basaltic
Trachy-Andesite
Trachy-
Basalt
Tephrite /
Basanite
NA
WA
ET
Alkaline
Tholeiitic
Foidite
Basalt
Basaltic
Andesite
Picro-Basalt
Na2O + K2O
SiO2
b.
Rhyolite
Dacite
WA
NA
Andesite
Basaltic-Andesite
ET
Foidite
Basalt
Alkali
Basalt
Zr/Ti
Nb/Y

Figure 7

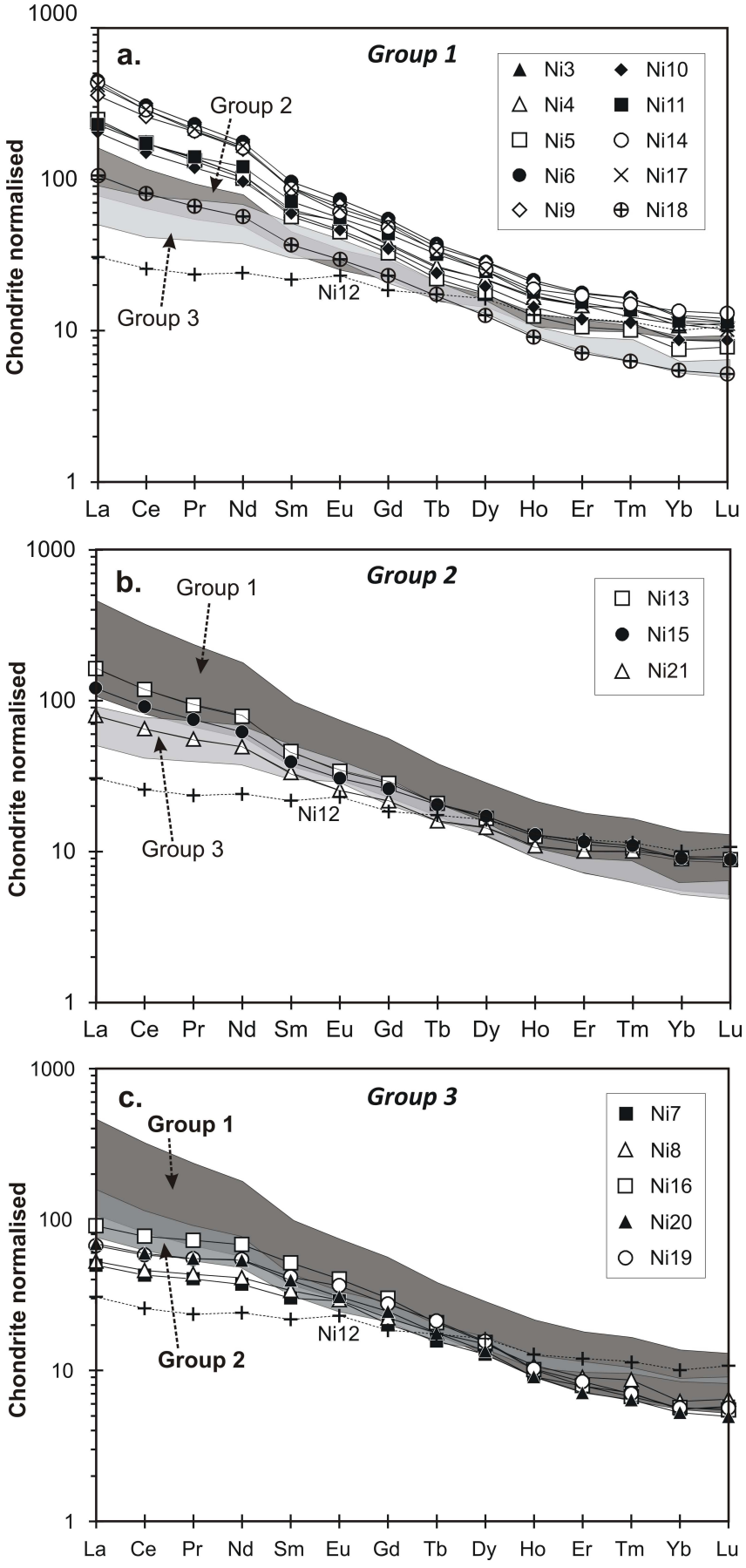
a.
Group 1
Group 2
Group 3
Ni12
Ni3
Ni4
Ni5
Ni6
Ni9
Ni10
Ni11
Ni14
Ni17
Ni18
Chondrite normalised
1000
100
10
1
La Ce Pr Nd Sm Eu Gd Tb Dy Ho Er Tm Yb Lu
b.
Group 2
Group 1
Group 3
Ni12
Ni13
Ni15
Ni21
c.
Group 3
Group 1
Group 2
Ni12
Ni7
Ni8
Ni16
Ni20
Ni19

Figure 8

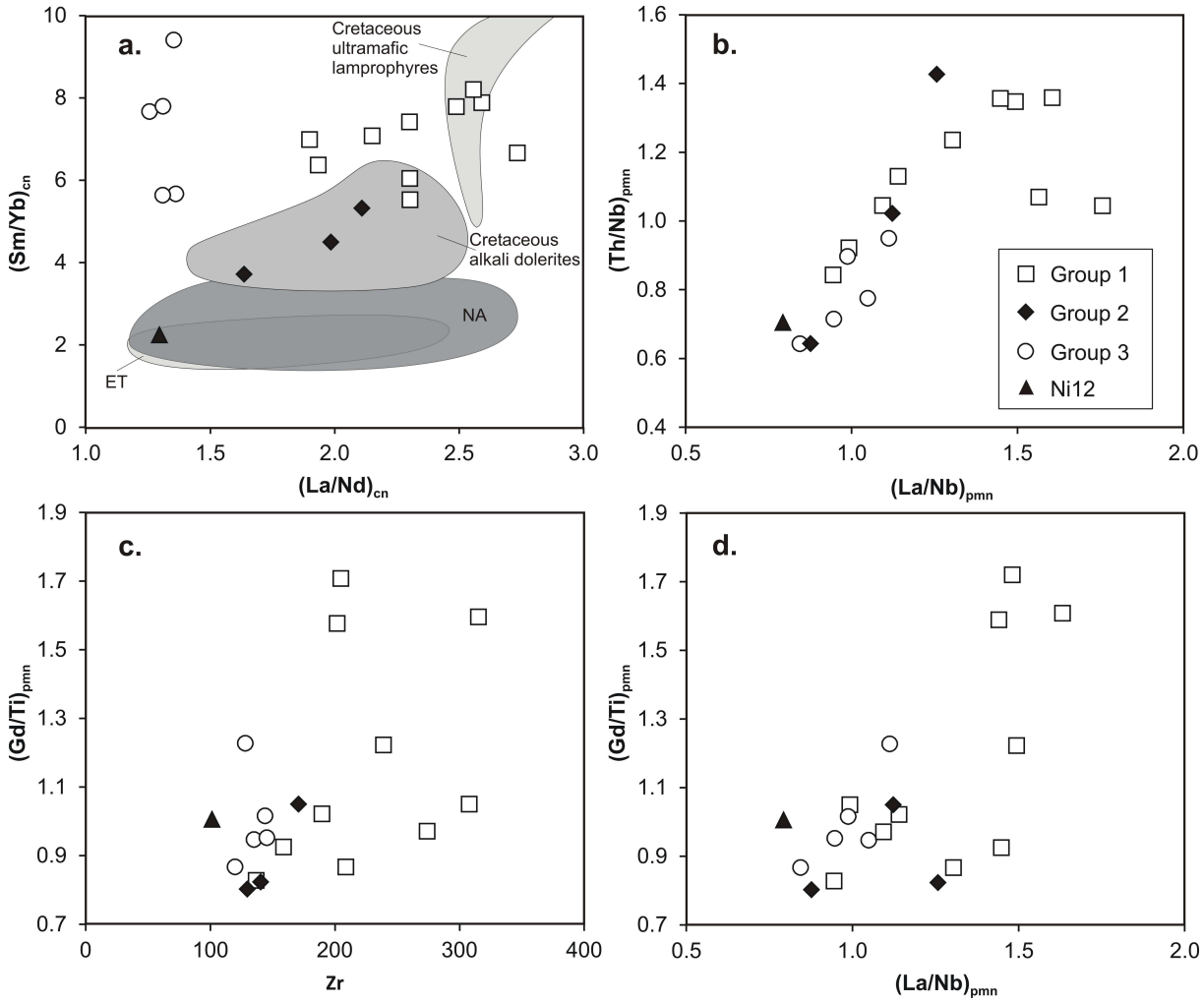
a.
Cretaceous ultramafic lamprophyres
Cretaceous alkali dolerites
NA
ET
(Sm/Yb)cn
(La/Nd)cn
b.
(Th/Nb)pmn
(La/Nb)pmn
Group 1
Group 2
Group 3
Ni12
c.
(Gd/Ti)pmn
Zr
d.
(Gd/Ti)pmn
(La/Nb)pmn

Figure 9

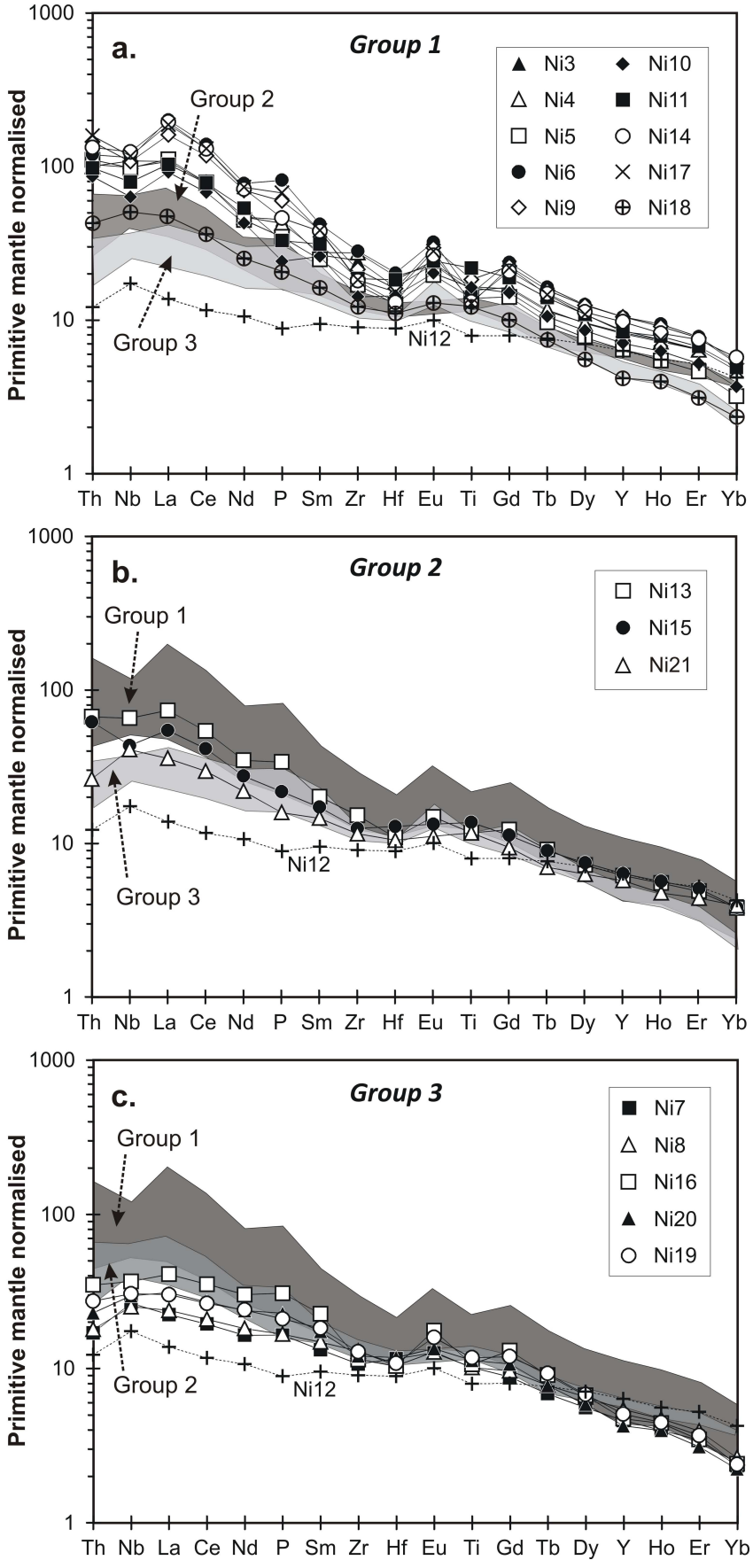
a.
Group 1
Group 2
Group 3
Ni12
Ni3
Ni4
Ni5
Ni6
Ni9
Ni10
Ni11
Ni14
Ni17
Ni18
b.
Group 2
Group 1
Group 3
Ni12
Ni13
Ni15
Ni21
c.
Group 3
Group 1
Group 2
Ni12
Ni7
Ni8
Ni16
Ni20
Ni19
Primitive mantle normalised
1000
100
10
1
Th Nb La Ce Nd P Sm Zr Hf Eu Ti Gd Tb Dy Y Ho Er Yb

Figure 10

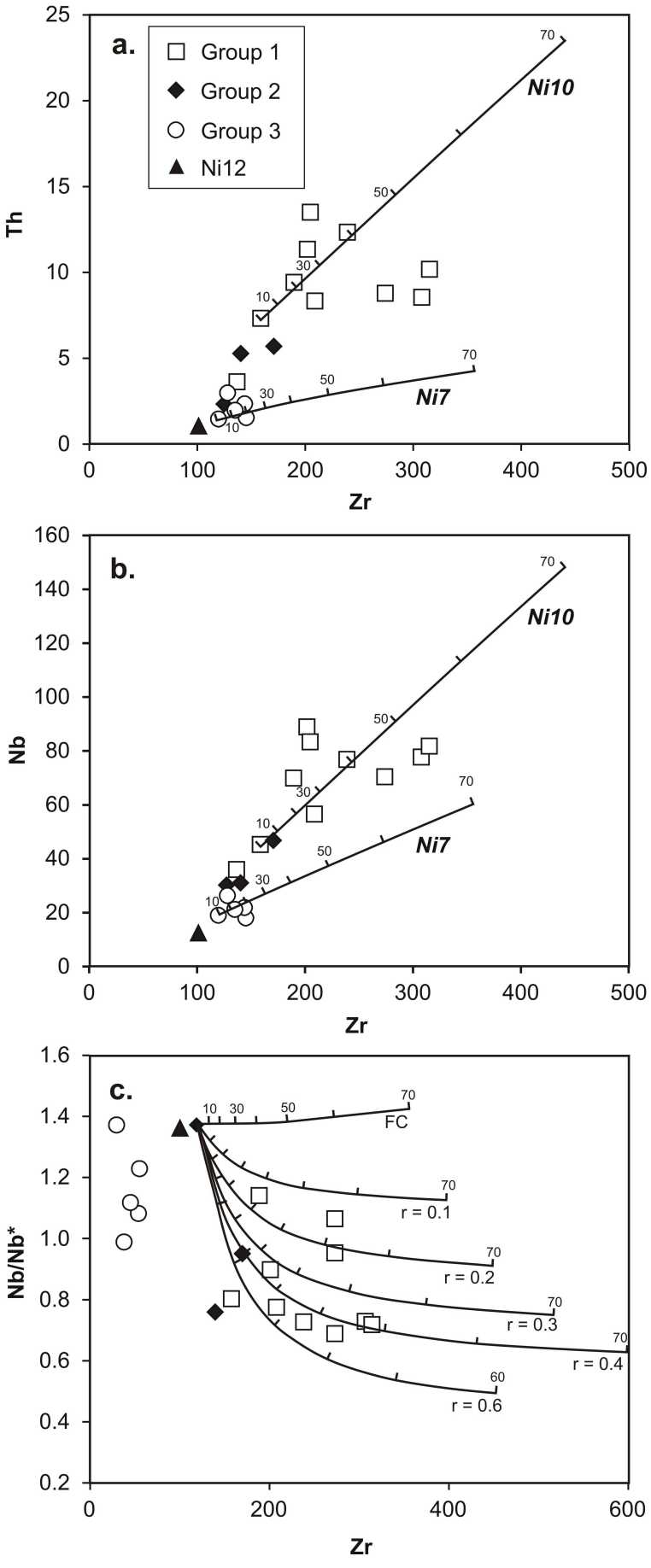
a.
Group 1
Group 2
Group 3
Ni12
Ni10
Ni7
Th
Zr
b.
Nb
c.
FC
r = 0.1
r = 0.2
r = 0.3
r = 0.4
r = 0.6
Nb/Nb*

Figure 11

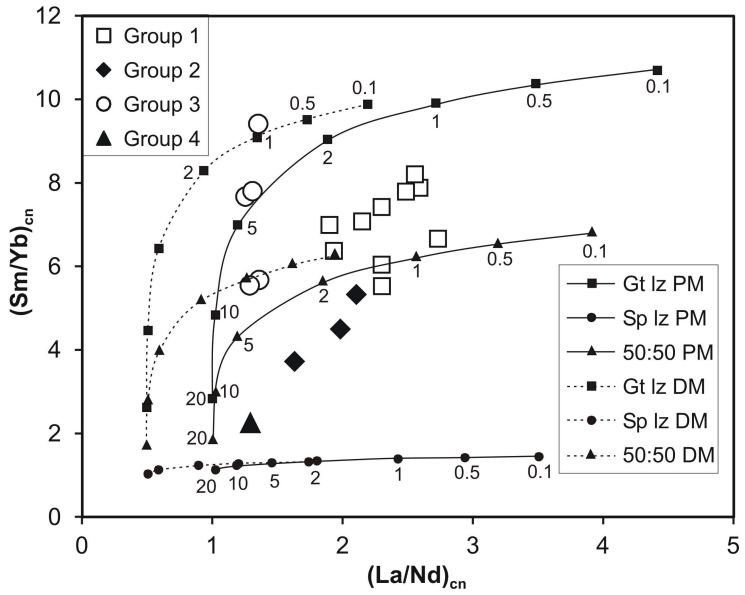
Group 1
Group 2
Group 3
Group 4
Gt lz PM
Sp lz PM
50:50 PM
Gt lz DM
Sp lz DM
50:50 DM
(Sm/Yb)cn
(La/Nd)cn
0
2
4
6
8
10
12
0
1
2
3
4
5
0.1
0.5
1
2
5
10
20

Figure 12

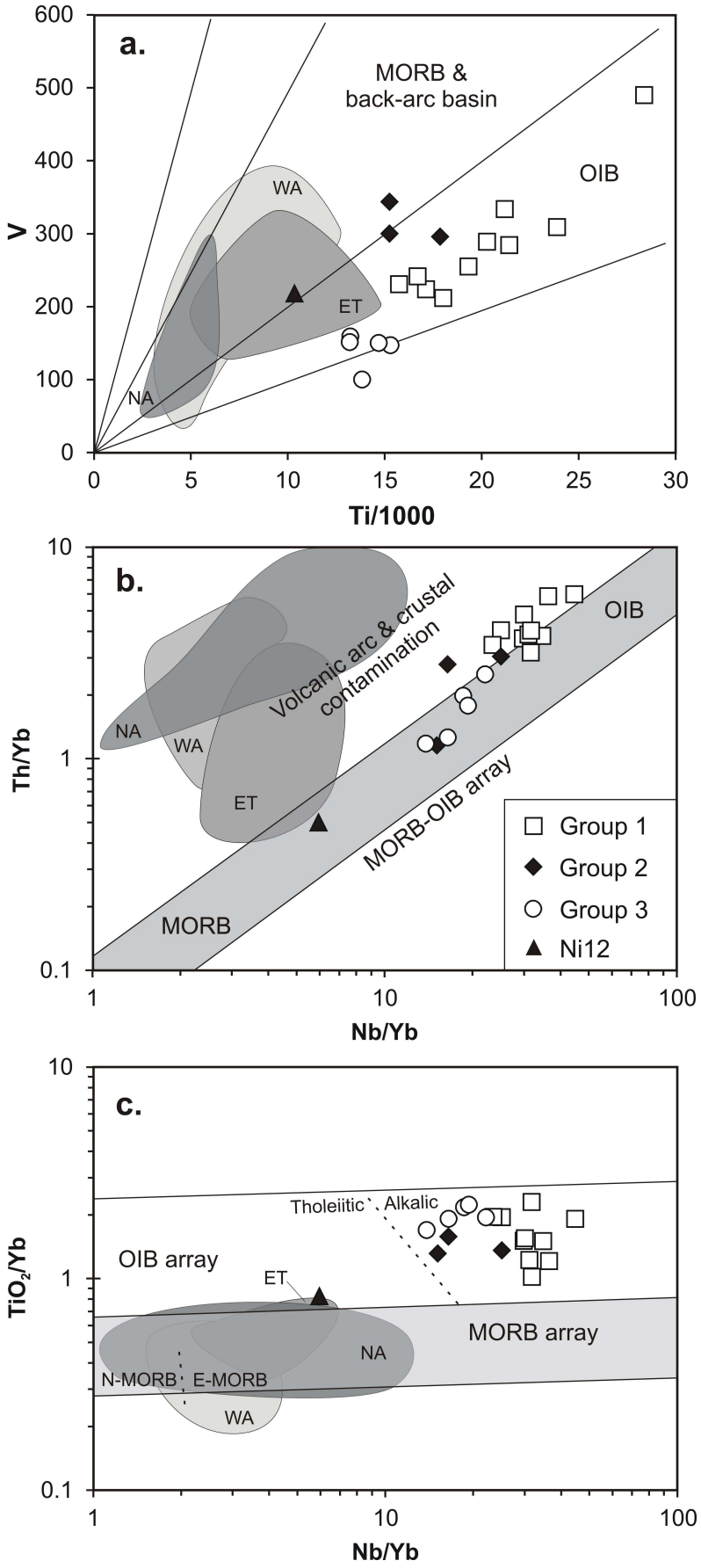
a.
MORB &
back-arc basin
OIB
WA
ET
NA
V
Ti/1000
b.
Volcanic arc & crustal
contamination
OIB
NA
WA
ET
MORB-OIB array
MORB
Group 1
Group 2
Group 3
Ni12
Th/Yb
Nb/Yb
c.
Tholeiitic
Alkalic
OIB array
ET
MORB array
NA
N-MORB
E-MORB
WA
TiO2/Yb
Nb/Yb

Figure 13

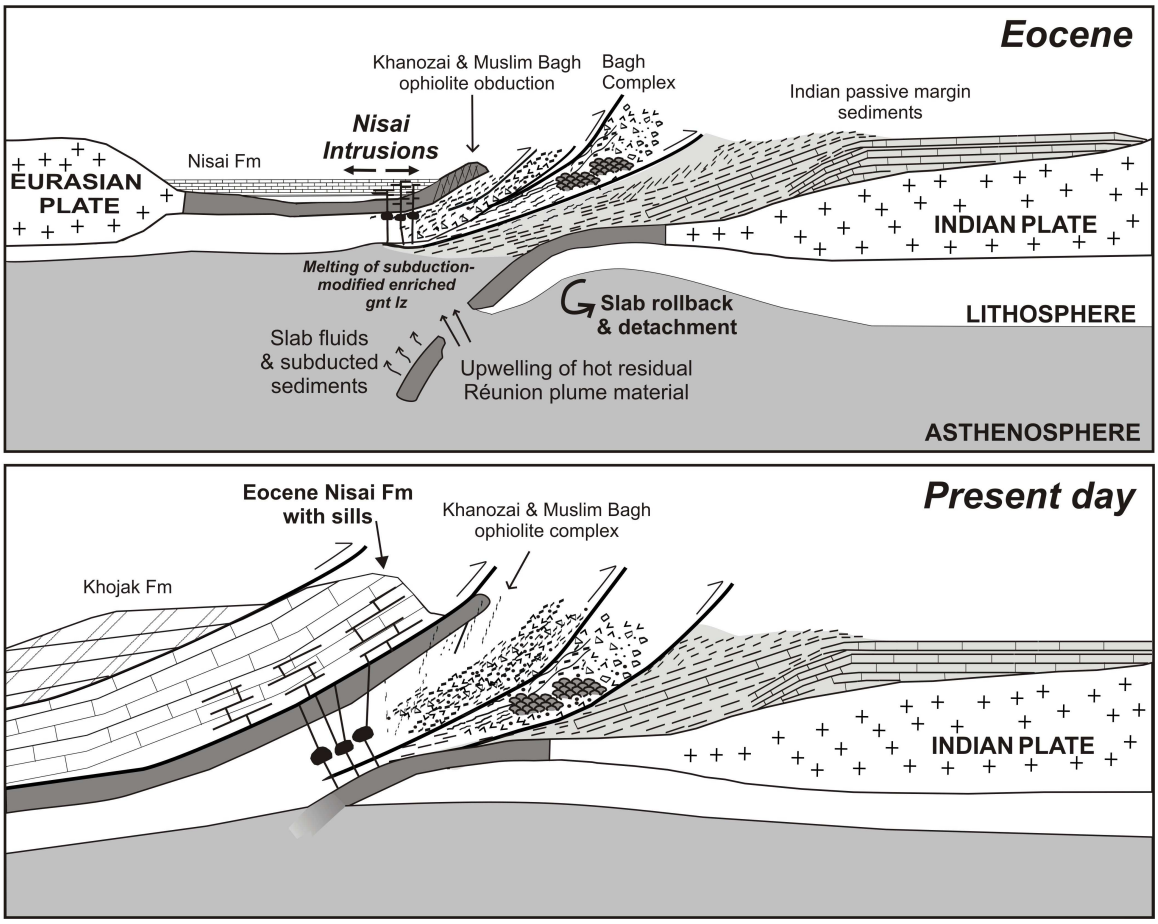
Eocene
Khanozai & Muslim Bagh ophiolite obduction
Bagh Complex
Indian passive margin sediments
Nisai Intrusions
Nisai Fm
EURASIAN PLATE
INDIAN PLATE
Melting of subduction-modified enriched gnt lz
Slab rollback & detachment
LITHOSPHERE
Slab fluids & subducted sediments
Upwelling of hot residual Réunion plume material
ASTHENOSPHERE
Present day
Eocene Nisai Fm with sills
Khanozai & Muslim Bagh ophiolite complex
Khojak Fm
INDIAN PLATE

Table 1 Major element and trace element analyses of the Nisai intrusions, Pakistan

	Ni3	NI4	Ni5	Ni6	Ni9	Ni10	NI11	NI14	Ni17	Ni18
	Group 1	Group 1	Group 1	Group 1	Group 1	Group 1	Group 1	Group 1	Group 1	Group 1
SiO_2	45.23	45.74	44.26	42.09	39.40	44.30	40.98	45.13	39.53	44.05
TiO_2	3.57	3.38	3.01	3.22	3.99	3.54	4.74	2.86	2.79	2.63
Al_2O_3	15.52	15.02	11.78	11.65	14.74	12.02	14.05	14.48	9.30	8.54
Fe_2O_3 (t)	13.16	12.98	11.56	14.64	14.19	12.95	15.66	12.88	13.60	12.81
MnO	0.23	0.20	0.24	0.25	0.22	0.18	0.18	0.23	0.23	0.18
MgO	7.89	6.51	15.85	9.92	9.10	10.70	9.45	8.71	17.02	14.05
CaO	7.80	10.65	9.83	12.90	11.60	12.92	10.07	11.32	12.88	14.23
Na_2O	3.73	4.18	1.44	2.64	3.83	2.80	2.67	2.98	0.08	0.65
K_2O	1.87	0.87	0.03	1.12	0.02	0.22	0.07	1.10	0.05	0.32
P_2O_5	0.982	0.929	0.758	1.776	1.299	0.526	0.717	1.004	1.470	0.447
LOI	0.77	0.42	1.60	0.48	1.24	0.85	0.90	0.40	2.31	1.70
Total	100.75	100.87	100.36	100.69	99.62	101.02	99.48	101.10	99.25	99.62
Sc	16.2	16.3	19.3	15.1	15.4	41.3	20.3	15.5	23.5	20.3
V	284	289	212	255	309	333	490	224	241	231
Cr	213	111	570	294	203	444	27	371	856	1187
Co	48	47	56	57	51	56	61	48	71	84
Ni	93	174	208	230	828	239	80	251	510	767
Cu	86	67	66	54	92	118	187	58	64	81
Zn	125	125	104	141	122	104	126	119	94	95
Ga	25.0	30.4	20.9	21.3	26.5	22.3	25.4	21.2	17.7	16.8
Rb	49.8	8.3	0.7	45.6	0.3	1.5	1.1	14.7	1.3	6.1
Sr	489	8220	528	1195	1138	811	837	3196	1422	1159
Y	37.8	37.0	29.3	47.7	47.7	32.2	38.2	44.3	38.9	19.0
Zr	274	308	190	315	239	159	209	202	205	137
Nb	70.42	77.72	69.86	81.74	76.80	45.27	56.54	88.94	83.38	36.00
Ba	586	449	40	585	50	183	142	511	585	330
La	74.22	74.32	76.78	138.33	110.55	63.19	71.07	134.07	128.94	32.77
Ce	139.07	139.06	139.68	247.24	209.06	120.55	138.86	231.12	232.00	64.98
Pr	16.86	16.72	16.13	28.15	25.20	14.49	17.13	25.45	26.21	8.08
Nd	63.51	63.63	60.79	105.19	94.67	57.90	72.42	96.65	99.34	34.00
Sm	11.80	12.23	11.02	18.72	17.15	11.55	13.87	16.85	17.02	7.18
Eu	3.90	3.85	3.29	5.41	4.97	3.40	4.08	4.43	4.72	2.17
Gd	9.54	9.76	8.44	14.14	13.39	8.99	11.28	12.38	13.08	5.97
Tb	1.23	1.26	1.04	1.77	1.69	1.14	1.51	1.61	1.58	0.80
Dy	7.08	7.01	5.67	9.28	9.19	6.30	8.04	8.31	8.01	4.06
Ho	1.21	1.19	0.89	1.55	1.49	1.03	1.29	1.35	1.22	0.65
Er	3.06	3.07	2.22	3.74	3.67	2.50	3.22	3.59	3.10	1.49
Tm	0.45	0.45	0.33	0.53	0.53	0.36	0.44	0.48	0.40	0.20
Yb	2.37	2.25	1.57	2.64	2.57	1.81	2.42	2.81	2.30	1.14
Lu	0.35	0.36	0.25	0.39	0.37	0.28	0.37	0.42	0.33	0.17
Hf	5.03	5.96	3.92	6.25	4.95	4.45	5.65	4.03	4.71	3.41
Ta	4.98	5.22	4.28	4.47	3.99	3.34	3.64	6.16	4.44	2.43
Pb	6.71	5.30	6.93	3.81	4.00	4.42	4.40	3.82	7.13	2.97
Th	8.77	8.54	9.41	10.17	12.33	7.32	8.33	11.34	13.50	3.62
U	2.63	2.39	2.15	3.15	2.27	1.37	1.45	4.17	2.97	0.93

Table 1 Major element and trace element analyses of the Nisai intrusions, Pakistan (cont)

	Ni13	**Ni15**	**Ni21**	**NI19**	**Ni20**	**Ni16**	**Ni7**	**Ni8**	**Ni12**
	Group 2	Group 2	Group 2	Group 3	Group 3	Group 3	Group 3	Group 3	
SiO_2	53.60	47.83	48.93	47.78	47.26	51.16	45.80	48.11	52.74
TiO_2	2.54	2.98	2.54	2.55	2.45	2.31	2.21	2.20	1.73
Al_2O_3	12.70	14.20	14.45	15.11	14.95	17.13	14.44	14.42	15.81
Fe_2O_3 t	10.23	13.56	14.08	11.98	15.43	11.11	14.69	13.27	11.59
MnO	0.09	0.26	0.20	0.21	0.12	0.11	0.17	0.14	0.12
MgO	5.43	8.51	7.85	3.83	7.46	3.19	9.28	5.94	7.04
CaO	5.78	7.97	6.70	10.13	6.96	6.71	8.03	8.82	3.77
Na_2O	7.54	2.91	3.98	5.86	3.76	7.31	3.83	4.63	4.87
K_2O	0.09	0.09	0.07	0.09	0.12	0.14	0.07	0.06	0.17
P_2O_5	0.739	0.474	0.346	0.458	0.498	0.671	0.359	0.364	0.194
LOI	0.50	1.38	1.25	1.09	1.38	0.66	1.06	1.34	1.05
Total	99.24	100.16	100.40	99.07	100.39	100.49	99.94	99.30	99.09
Sc	18.0	29.3	33.7	12.4	11.1	9.9	17.2	16.9	28.7
V	300	296	344	147	150	100	159	151	218
Cr	320	791	175	193	301	2	305	262	280
Co	37	63	55	38	59	28	52	51	45
Ni	683	1228	887	958	232	4	500	203	70
Cu	57	91	113	67	63	55	59	72	85
Zn	78	90	91	130	158	131	111	124	89
Ga	12.6	21.8	19.6	23.8	25.1	28.5	21.3	21.8	19.0
Rb	0.5	2.5	0.7	2.3	3.0	1.8	2.9	2.0	5.8
Sr	215	326	2193	377	295	394	290	314	524
Y	28.1	28.9	26.1	23.0	19.3	21.5	21.0	24.7	28.9
Zr	171	140	130	144	135	128	120	145	101
Nb	46.71	30.98	29.18	21.79	21.16	26.21	18.92	17.97	12.43
Ba	167	34	63	35	37	56	56	27	88
La	50.56	37.53	24.65	20.74	21.40	28.10	15.40	16.39	9.50
Ce	95.87	73.64	52.59	47.03	48.15	62.53	34.56	37.13	20.78
Pr	11.37	9.14	6.78	6.71	6.72	8.88	4.93	5.29	2.87
Nd	47.23	37.25	29.69	32.51	32.17	40.89	22.28	24.66	14.45
Sm	8.97	7.65	6.49	8.11	7.71	10.06	5.88	6.60	4.24
Eu	2.50	2.25	1.87	2.67	2.26	2.96	2.13	2.15	1.69
Gd	7.34	6.74	5.61	7.12	6.38	7.79	5.26	5.76	4.77
Tb	0.99	0.97	0.76	1.00	0.84	0.98	0.74	0.84	0.83
Dy	5.33	5.52	4.64	5.01	4.33	4.94	4.11	4.83	5.22
Ho	0.91	0.93	0.78	0.73	0.65	0.73	0.65	0.77	0.91
Er	2.34	2.44	2.12	1.77	1.50	1.66	1.66	1.89	2.51
Tm	0.34	0.35	0.33	0.23	0.21	0.22	0.23	0.28	0.37
Yb	1.87	1.89	1.94	1.18	1.10	1.19	1.15	1.30	2.10
Lu	0.28	0.28	0.29	0.18	0.16	0.18	0.19	0.21	0.35
Hf	3.38	3.99	3.25	3.34	3.65	3.21	3.58	3.23	2.75
Ta	3.83	2.20	1.74	1.62	1.57	2.06	1.19	1.25	0.69
Pb	3.30	3.55	2.57	7.39	4.93	7.79	2.33	1.74	3.38
Th	5.69	5.27	2.24	2.33	1.95	2.97	1.45	1.53	1.04
U	1.77	1.09	0.68	0.63	0.57	0.80	0.40	0.45	0.28

Table 2. Parameters used to model fractional crystallisation of the Nisai igneous intrusions.

Model	Pressure	H_2O content	Oxygen Buffer
Model 1	1 kbar	0%	QFM
Model 2	1 kbar	1%	QFM
Model 3	5 kbar	0%	QFM
Model 4	10 kbar	0%	QFM
Model 5	10 kbar	1%	QFM

QFM: Quartz-fayalite-magnetite oxygen buffer

Nisai Intrusions, Ziaba Section Khanozai area, northwestern Pakistan: sample locations and field notes

Sample no. Ni-03: Igneous intrusion in Nisai Formation near Churmian village. N 30° 43′ 20.3″E 067° 27′ 15. 2″. Altitude; 2225 metres.
Sample no. Ni-04: Igneous intrusion about 100 metres west of Ni-03 in Nisai Formation near Churmian village. N 30° 43′ 18.79″E 067° 27′ 14. 17″.

- **Samples Ni-3 & Ni-4 are 60m apart in a southerly direction.**
- **Located either side of a road/dried river bed.**

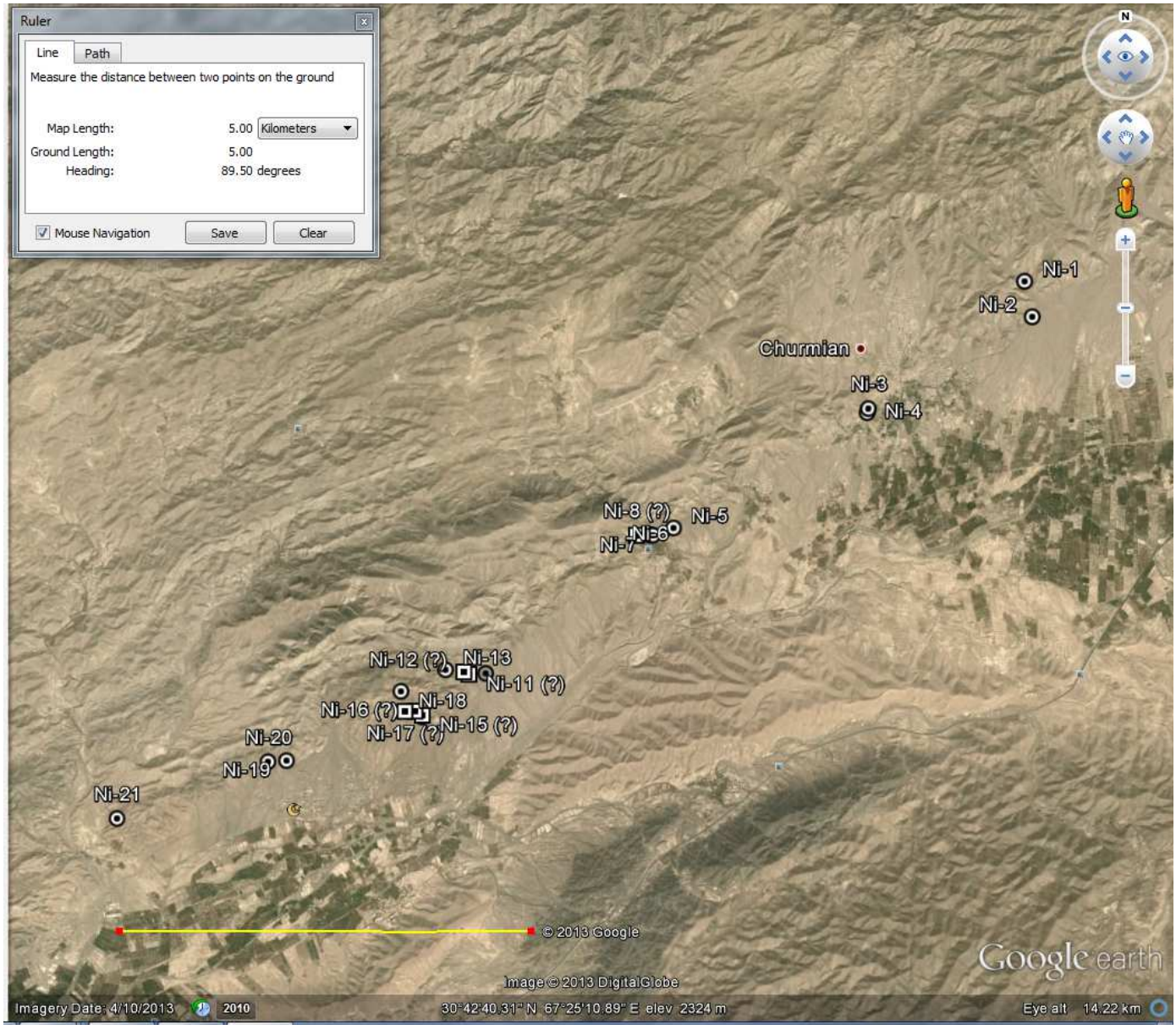

Sample no. Ni-05: Igneous intrusion in Nisai Formation near Zaiba village. N 30° 42′ 34.49″E 067° 25′ 48. 20″.
Sample no. Ni-06: Igneous intrusion in Nisai Formation near Zaiba village. N 30° 42′ 31.83″E 067° 25′ 37. 42″.
Sample no. Ni-07: Igneous intrusion in Nisai Formation within the Zaiba gorge near Zaiba village. N 30° 42′ 31.7″E 067° 25′ 39. 0″.

- **Samples Ni-6 & Ni-7 are found in very close proximity (40m apart) on the sample hillside.**
- **Zaiba village is directly to the south of this location and the Zaiba gorge to directly to the west (70m downslope SW of Ni-6).**

Sample no. Ni-08: Igneous intrusion about 200 metres west of Ni-07 in the Nisai Formation, Zaiba Gorge near Zaiba village.

- **NO COORDINATES**

- **Approximately 200m of Ni-7, therefore has been approximated on map (square marker). Located on opposite side of the 'Zaiba gorge' from Ni6 & 7.**

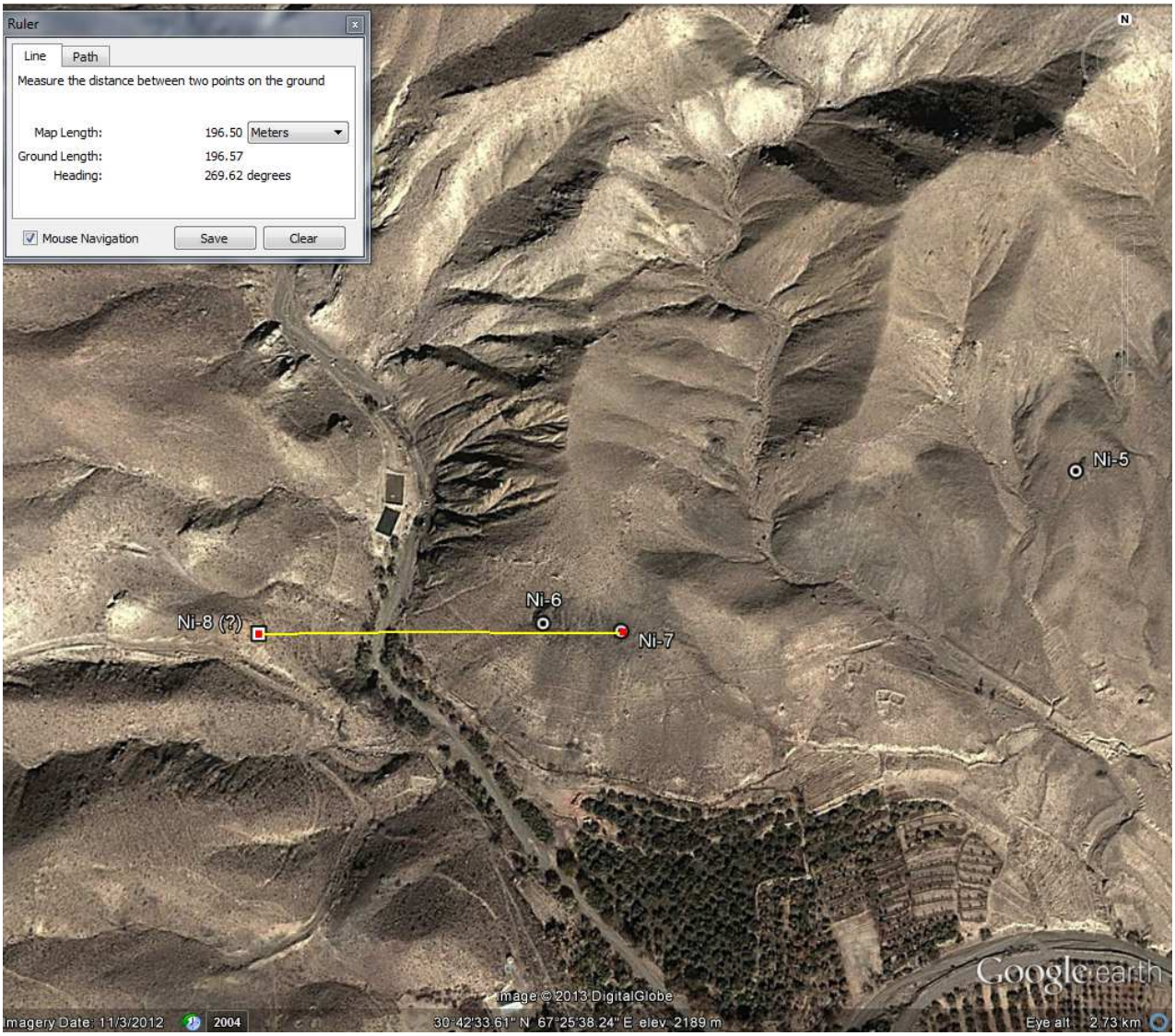

Sample no. Ni-09: Igneous intrusion in Nisai Formation southwest of Zaiba village. N 30° 41′ 38.2″E 067° 24′ 23. 8″. Altitude; 2125 metres.
Sample no. Ni-10: Igneous intrusion nearby the sample no. Ni-08 in Nisai Formation southwest of Zaiba village. N 30° 41′ 38.2″E 067° 24′ 23. 8″. Altitude; 2125 metres.

Sample no. Ni-11: Igneous intrusion about 200 metres west of Ni-09 & Ni-10 in Nisai Formation, in the area between Zaiba and Murgha Zakaryazai village.
Sample no. Ni-12: Igneous intrusion about 70 metres northwest of Ni-11 in Nisai Formation, in the area between Zaiba and Murgha Zakaryazai village.

- **Villages are not located on Google earth so cannot use for exact reference.**

Sample no. Ni-13: Igneous intrusion about 300 metres west of Ni-07 & Ni-08 in Nisai Formation, in the area between Zaiba and Murgha Zakaryazai village. N 30° 41′ 39.7″E 067° 24′ 05. 9″. Altitude; 2144 metres.

- **Located within a dried river bed… prominent feature directly to the west of these coordinates indicates the igneous intrusion.**

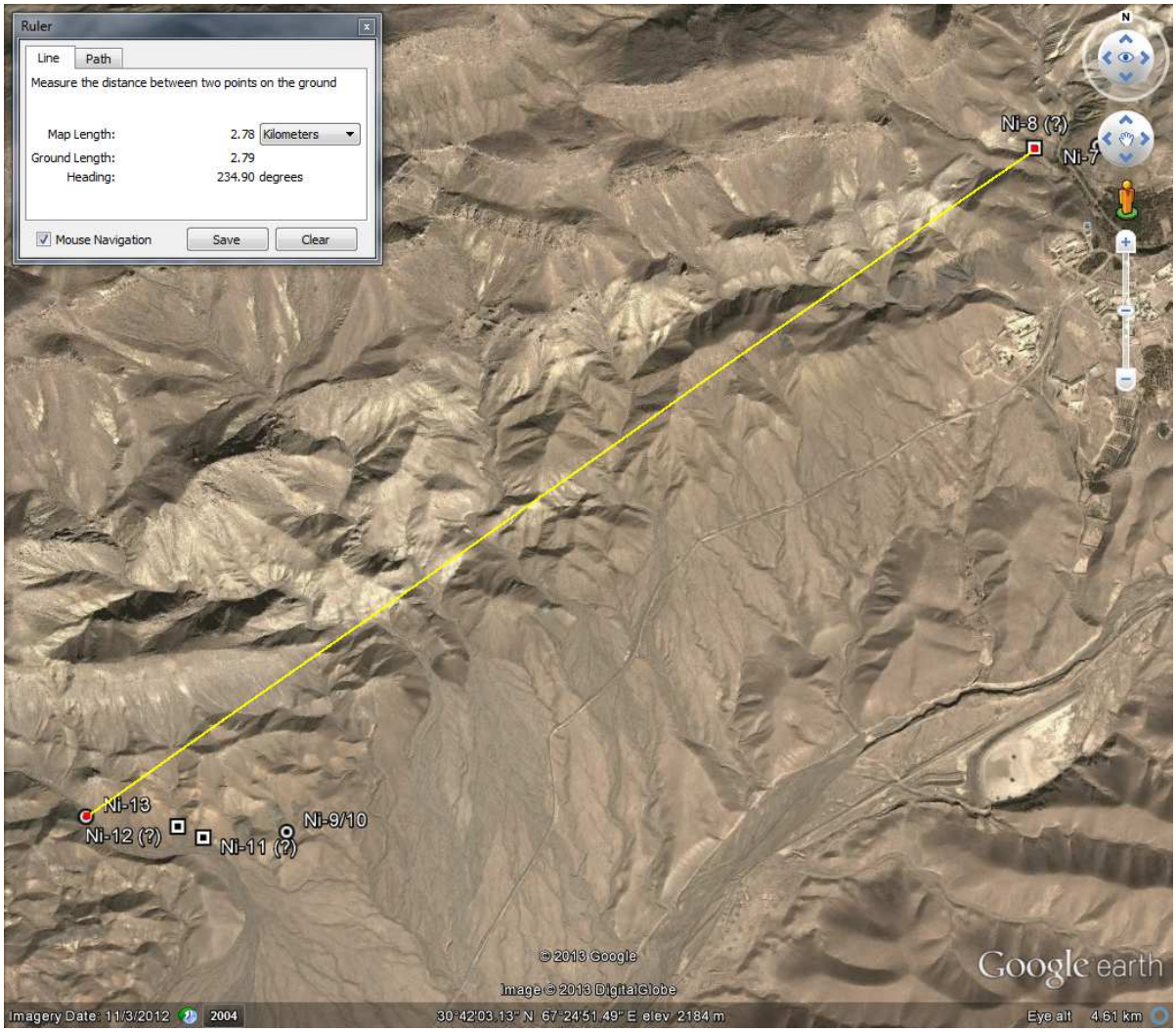

Sample no. Ni-14: Igneous intrusion in lower shaley part of Nisai Formation up stream of the Murgha Zakaryazai high school. N 30° 41′ 21.11″E 067° 23′ 55. 07″.

Sample no. Ni-15: Fine-grained dolerite? About 20 m north of Ni-14 in lower shaley part of Nisai Formation up stream of the Murgha Zakaryazai high school.
Sample no. Ni-16: Course-grained dolerite? About 100 m northwest of Ni-15 in lower shaley part of Nisai Formation upstream the Murgha Zakaryazai high school.
Sample no. Ni-17: Dolerite? About 120 m west of Ni-16 in lower shaley part of Nisai Formation up stream of the Murgha Zakaryazai high school.

- **Ni-15 is directly up-valley from Ni-14**
- **Ni-16 is on a separate hillside.**
- **Ni-17 sampled within a dried river bed**

Sample no. Ni-18: Fine-grained dolerite? About 30 m west of Ni-17 in lower shaley part of Nisai Formation up stream of the Murgha Zakaryazai high school. N 30° 41′ 31.43″E 067° 23′ 45. 88″.

- **Located at the top of the water-shed for the dried river.**

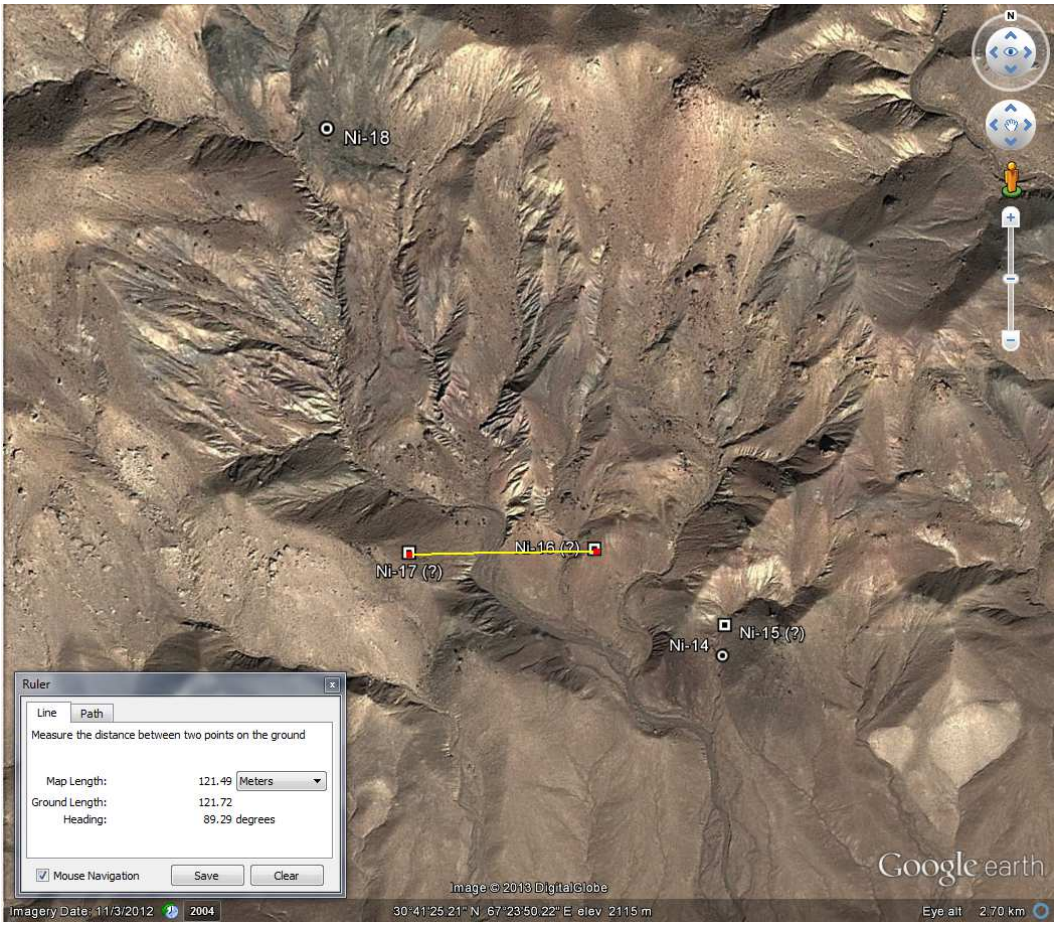

Sample no. Ni-19: Igneous intrusion in Nisai Formation on the top of Murgha Zakaryazai village. N 30° 41′ 03.85″E 067° 22′ 53. 3″. Altitude; 2011 metres.
Sample no. Ni-20: Igneous intrusion in Nisai Formation on the top of Murgha Zakaryazai village. N 30° 41′ 03.4″E 067° 22′ 44.9. Altitude; 2055 metres.

- **Both located in a similar location, 220m apart on separate hillsides.**

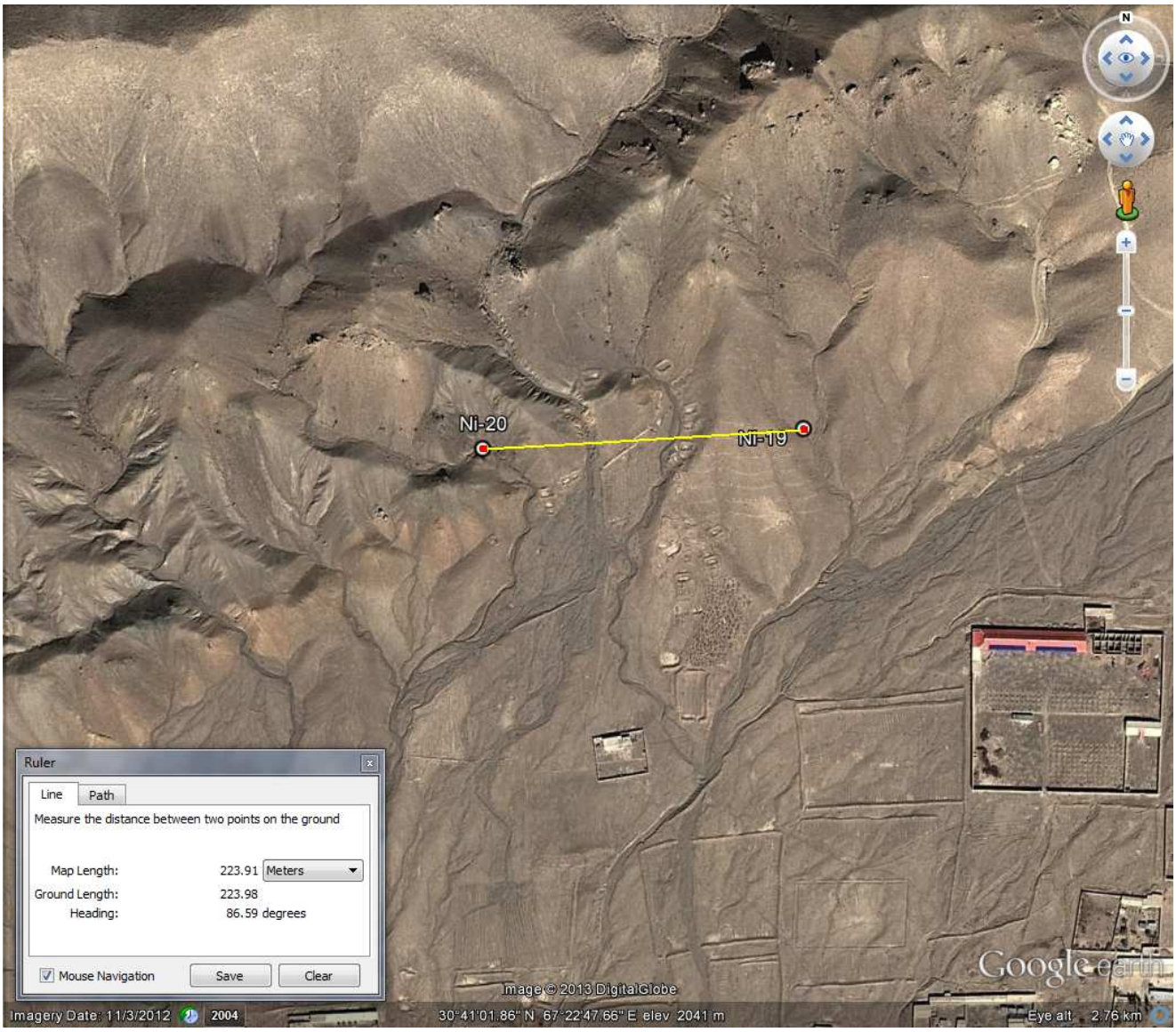

Sample no. Ni-21: Igneous intrusion in Nisai Formation near Nareen village. N 30° 40′ 41.1″E 067° 21′ 36.2. Altitude; 2052 metres.

- **Ni-21 is located on the summit of a prominent feature in the landscape.**

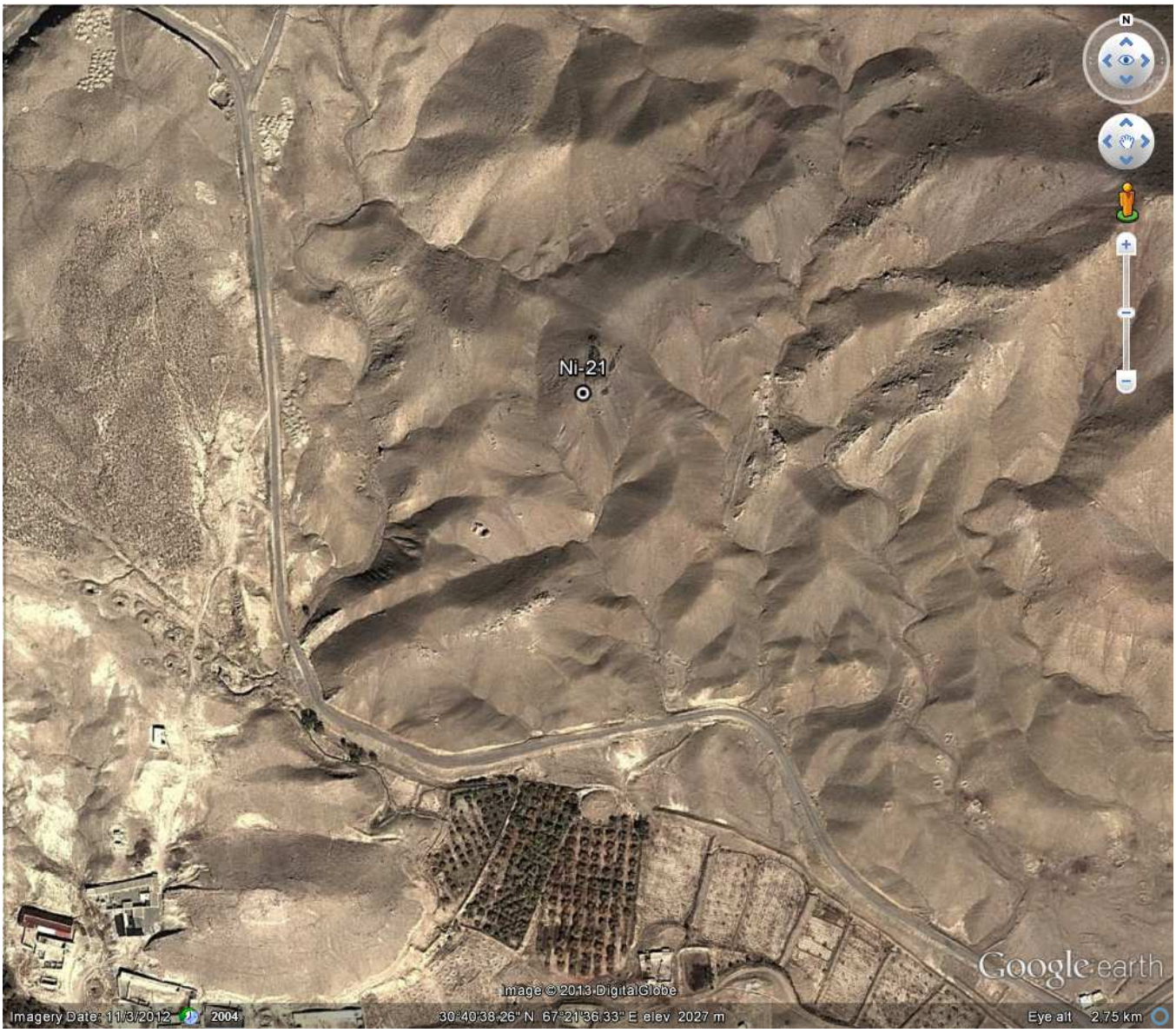
Ni-21
Image © 2013 DigitalGlobe
Google earth
Imagery Date: 11/3/2012
2004
30°40'38.26" N 67°21'36.33" E elev 2027 m
Eye alt 2.75 km

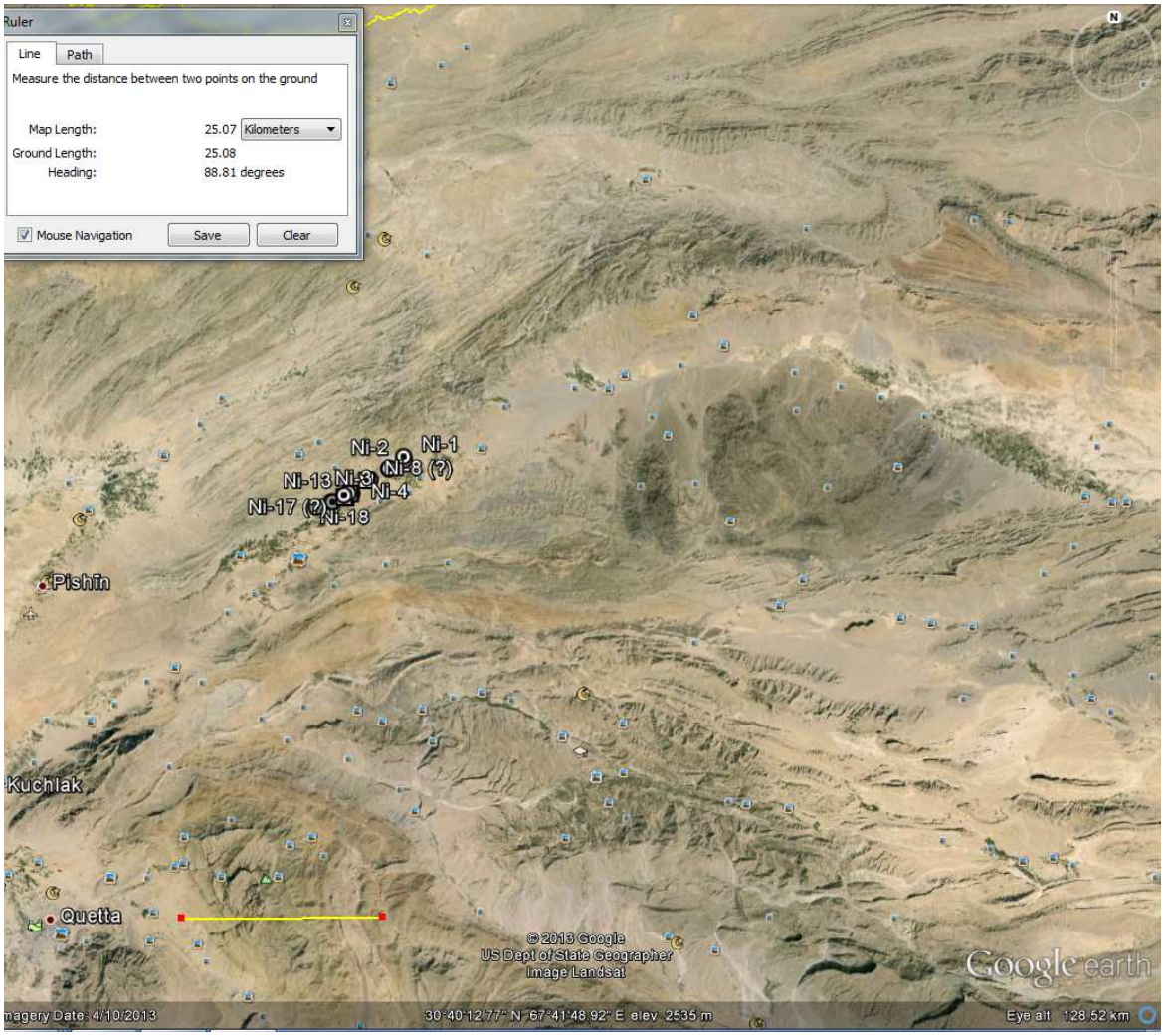
Ruler
Line
Path
Measure the distance between two points on the ground
Map Length: 25.07 Kilometers
Ground Length: 25.08
Heading: 88.81 degrees
Mouse Navigation
Save
Clear
Ni-1
Ni-2
Ni-8 (?)
Ni-13
Ni-3
Ni-4
Ni-17 (?)
Ni-18
Pishin
Kuchlak
Quetta
© 2013 Google
US Dept of State Geographer
Image Landsat
Google earth
Imagery Date: 4/10/2013
30°40'12.77" N 67°41'48.92" E elev 2535 m
Eye alt 128.52 km

Online Appendix 2 - International reference materials JB-1A /BIR-1 analysed during the course of the study

	STANDARD RUNS						STANDARD RUNS			
	JB-1A					BIR-1				
	1	2	3	4	5		1	2	3	4
SiO_2	52.32	52.68	52.10	52.61	52.31	SiO_2	47.67	46.13	47.51	47.99
TiO_2	1.28	1.29	1.25	1.29	1.30	TiO_2	0.94	0.96	0.95	0.95
Al_2O_3	14.01	14.56	14.34	14.50	14.84	Al_2O_3	15.41	14.97	15.11	15.07
$Fe_2O_3(t)$	9.10	9.15	9.13	9.11	8.66	$Fe_2O_3(t)$	11.17	11.36	11.67	11.05
MnO	0.14	0.14	0.14	0.14	0.14	MnO	0.17	0.17	0.17	0.17
MgO	7.92	7.91	8.30	7.65	7.94	MgO	9.64	9.69	9.48	9.40
CaO	9.54	9.42	9.54	9.17	9.20	CaO	13.24	13.90	13.03	12.71
Na_2O	2.68	2.71	2.67	2.77	2.69	Na_2O	1.72	2.25	1.77	1.80
K_2O	1.32	1.33	1.39	1.42	1.42	K_2O	0.02	0.03	0.04	0.02
P_2O_5	0.26	0.27	0.24	0.27	0.26	P_2O_5	0.02	0.12	0.04	0.02
Sc	27.6	27.9	27.8	27.7	26.1	Sc	44.4	46.4	41.5	39.7
V	201.9	197.1	214.4	210.8	205.0	V	320.5	306.3	330.6	312.9
Cr	425.1	431.1	421.3	429.7	418.0	Cr	399.3	397.5	388.0	375.8
Co	38.9	38.8	36.6	38.7	36.8	Co	52.9	50.2	50.6	49.6
Ni	197.2	140.9	145.2	137.1	138.9	Ni	173.4	167.6	160.7	180.3
Ga	17.6	18.3	17.6	18.0	17.9	Ga	15.2	15.3	14.6	15.1
Rb	43.5	40.3	39.9	36.9	41.5	Rb	0.3	0.3	0.2	0.2
Sr	441.4	452.0	439.6	447.9	441.3	Sr	105.1	109.6	105.3	100.9
Y	24.0	24.6	24.2	25.1	24.0	Y	15.7	16.5	15.8	15.6
Zr	142.5	143.6	146.3	146.0	148.4	Zr	16.2	15.6	15.3	16.7
Nb	27.98	28.02	27.24	28.06	27.57	Nb	0.59	0.61	0.46	0.58
Ba	482.5	508.2	501.6	487.9	490.3	Ba	14.5	57.6	2.4	7.8
Hf	3.41	3.52	3.43	3.44	3.52	Hf	0.54	0.58	0.55	0.53
Ta	1.69	1.71	1.71	1.68	1.70	Ta	0.04	0.04	0.03	0.04
Th	8.94	9.04	8.84	8.77	8.67	Th	0.05	0.09	0.08	0.06
U	1.59	1.72	1.67	1.68	1.68	U	0.02	0.02	0.01	0.02
La	37.50	38.87	37.41	37.62	37.19	La	0.63	0.67	0.48	0.64
Ce	63.95	66.78	63.19	65.86	66.39	Ce	1.89	1.88	1.96	1.97
Pr	7.11	7.20	7.12	7.06	7.06	Pr	0.35	0.37	0.34	0.38
Nd	25.57	27.40	25.56	25.30	26.43	Nd	2.50	2.35	2.08	2.38
Sm	4.97	5.30	4.99	5.03	5.07	Sm	1.08	1.09	0.98	1.06
Eu	1.48	1.65	1.47	1.49	1.48	Eu	0.54	0.52	0.52	0.49
Gd	4.58	4.86	4.71	4.64	4.67	Gd	1.79	1.69	1.75	1.64
Tb	0.67	0.71	0.68	0.71	0.69	Tb	0.36	0.33	0.33	0.33
Dy	3.93	4.26	3.97	4.10	4.05	Dy	2.54	2.46	2.46	2.42
Ho	0.72	0.73	0.72	0.74	0.74	Ho	0.57	0.51	0.54	0.51
Er	2.07	2.20	2.08	2.08	2.10	Er	1.68	1.55	1.64	1.55
Tm	0.32	0.33	0.32	0.33	0.32	Tm	0.26	0.25	0.24	0.25
Yb	2.07	2.12	2.06	2.07	2.10	Yb	1.64	1.63	1.63	1.62
Lu	0.32	0.33	0.32	0.32	0.32	Lu	0.27	0.26	0.26	0.26